The Astrophysical Journal, 744:106 (18pp), 2012 January 10 doi:10.1088/0004-637X/744/2/106

A MAGNETAR-LIKE EVENT FROM LS I +61°303 AND ITS NATURE AS A GAMMA-RAY BINARY

Diego F. Torres[1,2], Nanda Rea[1], Paolo Esposito[3], Jian Li[4], Yupeng Chen[4], and Shu Zhang[4]
[1] Institut de Ciències de l'Espai (IEEC-CSIC), Campus UAB, Torre C5, 2a planta, 08193 Barcelona, Spain
[2] Institució Catalana de Recerca i Estudis Avançats (ICREA), 08010 Barcelona, Spain
[3] INAF, Osservatorio Astronomico di Cagliari, località Poggio dei Pini, strada 54, I-09012 Capoterra, Italy
[4] Key Laboratory of Particle Astrophysics, Institute of High Energy Physics, Chinese Academy of Science, Beijing 100049, China
Received 2011 June 7; accepted 2011 September 22; published 2011 December 20

ABSTRACT

We report on the *Swift* Burst Alert Telescope detection of a short burst from the direction of the TeV binary LS I +61°303, resembling those generally labeled as magnetar-like. We show that it is likely that the short burst was indeed originating from LS I +61°303 (although we cannot totally exclude the improbable presence of a far-away, line-of-sight magnetar) and that it is a different phenomenon with respect to the previously observed ks-long flares from this system. Accepting the hypothesis that LS I +61°303 is the first magnetar detected in a binary system, we study those implications. We find that a magnetar-composed LS I +61°303 system would most likely be (i.e., for the usual magnetar parameters and mass-loss rate) subject to a flip-flop behavior, from a rotationally powered regime (in the apastron) to a propeller regime (in the periastron) along each of the LS I +61°303 eccentric orbital motion. We prove that, unlike near an apastron, where an interwind shock can lead to the normally observed LS I +61°303 behavior, during TeV emission the periastron propeller is expected to efficiently accelerate particles only to sub-TeV energies. This flip-flop scenario would explain the system's behavior when a recurrent TeV emission only appears near the apastron, the anti-correlation of the GeV and TeV emission, and the long-term TeV variability (which seems correlated to LS I +61°303's super-orbital period), including the appearance of a low TeV state. Finally, we qualitatively put the multi-wavelength phenomenology into the context of our proposed model and make some predictions for further testing.

Key words: stars: magnetars – X-rays: binaries – X-rays: individual (LSI+61303)

Online-only material: color figures

1. INTRODUCTION

Besides highly energetic, rotationally powered pulsars, there are only a handful of other classes of Galactic objects known to emit at GeV–TeV energies, e.g., high-mass X-ray binaries (HMXBs).

The first identified TeV binary system was a 3.4 yr period binary hosting a 48 ms radio pulsar in an eccentric orbit around a Be star, PSR B1259–63 (Johnston et al. 1992; Aharonian et al. 2005). The emission from this object is thought to be associated with the radio-pulsar wind and its interaction with the radiation field and/or the material surrounding the Be star. It shows variable radio-to-TeV emission (Johnston et al. 1999, 2005; Chernyakova et al. 2006, 2009; Tam et al. 2011; Abdo et al. 2011). The other two TeV-emitting systems, LS I +61°303 and LS 5039, are both much closer binaries, with orbital periods of 26.5 and 3.9 days, respectively, hosting a very massive star (Be and O types) and a compact object, the nature of which is still unknown. They are also both variable, from the radio to the TeV energy range, often showing their orbital modulation throughout the multi-wavelength energy spectrum (e.g., see Abdo et al. 2009a, 2009b; Aharonian et al. 2006; Albert et al. 2008, 2009; Torres et al. 2010; Li et al. 2011). Their X-ray emission showed ks-timescale flares (Sidoli et al. 2006; Esposito et al. 2007; Rea et al. 2010; Li et al. 2011), and is characterized in both of the objects by an absorbed power-law spectrum.

Very recently, other HMXBs emitting at high energies have been confirmed. On the one hand, we know of HESS J0632+057 (Aharonian et al. 2007; Hinton et al. 2009). This system again hosts a Be star in orbit with a compact object of unknown nature. This TeV binary has an orbital period of 320 days (Bongiorno et al. 2011), and again shows radio and X-ray variability (Falcone et al. 2010; Skilton et al. 2009; Rea & Torres 2011). No GeV emission has been observed from HESS J0632+057 yet. On the other hand, *Fermi* Large Area Telescope (LAT) observations of the gamma-ray source 1FGL J1018.6−5856 revealed the presence of periodic modulation with a period of 16.5 days (Corbet et al. 2011). Optical observations found an O6V(f) star that was very similar to that of the gamma-ray binary LS 5039, which coincides with a variable X-ray and radio source. This led to the conclusion that 1FGL J1018.6−5856 is a new member of the rare gamma-ray binary class because it shared several similarities with LS 5039. In the latter case, no TeV emission has yet to be reported.

But what is the physical nature of these binaries? Two physical scenarios have been put forward (see, e.g., Mirabel 2006). On the one hand, a compact object rotating around the massive companion star drives relativistic jets as a result of accretion. The gamma-ray binaries would thus be microquasars (see, e.g., Bosch-Ramon & Khangulyan 2009 for a review). On the other hand, the compact object could be a rotationally powered pulsar that drives a wind (e.g., Maraschi & Treves 1981). There are two types of models in this case. The interwind models are those where the acceleration of the electron population, which is primary to the gamma-rays observed, originates in the shock region resulting from the interaction of the pulsar and stellar winds (see, e.g., Dubus 2006a). Instead, the physical scenario for high-energy photon production in intrawind models is as follows: pairs are injected by the pulsar or inner-wind shocks and travel toward the observer, producing inverse Compton (IC) photons via the up-scattering of thermal photons from the massive star. Gamma-ray photons can initiate an IC cascade due to absorption in the same thermal field in both cases (see, e.g., Sierpowska-Bartosik & Torres 2008). Models for gamma rays with pulsars as compact objects have been recently discussed by Torres (2011).

In the last few decades, two classes of pulsars have received increasing interest: the soft gamma repeaters (SGRs) and the anomalous X-ray pulsars (AXPs). They are two peculiar groups of neutron stars that stand apart from other known classes of X-ray pulsars. In particular, their X-ray luminosities are often larger than the values expected from tapping their rotational power reservoir ($L \sim 10^{35}$ erg s^{-1}), and they show no evidence for a companion star that could power this strong emission via accretion. Their rotational periods (2–12 s) and period derivatives ($\sim 10^{-13}$–10^{-11} s s^{-1}), for most of the $\sim$20 sources known to date, point to a magnetic field of $\sim 10^{14}$–10^{15} G, which is currently believed to be responsible for their peculiar emission properties (see Rea & Esposito 2011 and Mereghetti 2008 for recent reviews). At present, in fact, the model that most successfully explains the emissions of the SGRs and AXPs is the "magnetar" model: these objects are thought to be strongly magnetized (isolated) neutron stars emitting across all wavelengths via the decay and the instabilities of their high B-fields (Duncan & Thompson 1992; Thompson & Duncan 1993).

The most peculiar and intriguing property of the SGRs and AXPs are their outbursts and flares, which differ from any other bursting event observed so far in other compact objects. In particular, the unpredictable flaring activity of the magnetars can be phenomenologically classified in a few types.

1. *X/γ-ray short bursts*. These are the most common and less energetic flaring events. They have short durations ($\sim$0.01–0.2 s), thermal spectra, and peak luminosities of $\sim 10^{38}$–10^{41} erg s^{-1}, and they can occur randomly as single events or in a bunch (see recent examples in Rea et al. 2009; Kumar et al. 2010).
2. *Intermediate flares*. They are intermediate both in duration and luminosity between short bursts (1) and the giant flares we discuss below. They have durations ranging between $\sim$2–60 s and luminosities of $\sim 10^{41}$–10^{43} erg s^{-1}. Sometimes intermediate flares last longer than the pulsars' spin periods and show a clear modulation at the star rotational period (see recent examples in Israel et al. 2008; Mereghetti et al. 2009).
3. *Giant flares*. They are by far the most energetic ($\sim 10^{43}$–10^{47} erg s^{-1}) Galactic events after supernova explosions. So far, we have detected only three of these events, which are characterized by a very luminous hard peak lasting less than 1 s, and by decaying tails lasting 100–500 s where the spin period of the neutron star is clearly visible.
4. *Outbursts*. They are enhancements of the multi-band emission of the SGRs and AXPs by a factor of 5–1000, with a typical total energy release of $\sim 10^{40}$–10^{45} erg. The increase flux level of the source may last from a few months up to several years (see Israel & Dall'Osso 2011 and Rea & Esposito 2011 for a recent review on the flaring activity of magnetars).

All of the above flaring events are peculiar to and defining of the *magnetar* class.

In this paper, we provide a complete analysis of a magnetar-like short burst detected by the Burst Alert Telescope (BAT; Barthelmy et al. 2008) on board *Swift* from the direction of the TeV binary LS I $+61^{\circ}303$. The event prompted several instant notices (Astronomer Telegrams and Gamma-ray bursts Coordinate Network circulars): the *Swift*/BAT trigger was reported by De Pasquale et al. (2008), the *Swift*/BAT localization by Barthelmy et al. (2008), and Evans et al. (2008) noticed that a quasi-simultaneous follow-up with the *Swift* X-ray Telescope (XRT) unveiled only one source within the burst error circle: LS I $+61^{\circ}303$. Furthermore, brief interpretational comments and reports of multi-wavelength observations discussing the magnetar-like features of the burst were posted (Dubus & Giebels 2008; Rea & Torres 2008, and Muñoz-Arjonilla et al. 2008).

To understand the nature of this short burst, the *Swift*/BAT data were reanalyzed, as were those of various *Rossi X-ray Timing Explorer* (*RXTE*) and *Chandra* observations of the field of LS I $+61^{\circ}303$. In particular, the data collected by the *RXTE* simultaneously with its Proportional Counter Array (PCA) and High-Energy X-Ray Timing Experiment (HEXTE) allow us to explore a possible alternative origin for the burst, namely the possibility of it being the result of a spectral evolution in a longer (normal) flare. All of our observational analyses are presented in Section 2. In Section 3 we compare the *Swift*/BAT burst with those observed from known magnetars, showing in detail the striking similarity with the detection of interest in this paper. In Section 4 we confront the hypothesis that LS I $+61^{\circ}303$ might indeed host a magnetar and explore its implications. In Section 6, we discuss our results and the proposed model resulting from the previous sections on the light of the multi-band variable emission of LS I $+61^{\circ}303$; we reinterpret all of the observations from the radio and TeV gamma rays and note the possibility of having evidence of the first magnetar in a binary system.

2. OBSERVATIONS AND ANALYSIS

2.1. *Swift*/BAT: A Magnetar-like Burst

The BAT (Barthelmy et al. 2008), which is the hard X-ray detector on board the *Swift* (Gehrels et al. 2004), is a highly sensitive, coded mask instrument optimized for the 15–150-keV energy range. It was specifically designed to catch and study prompt emission from gamma-ray bursts and other interesting high-energy transients.

On 2008 September 10 at 12:52:21 UT, the *Swift*/BAT triggered on a burst in the direction of the gamma-ray binary LS I $+61^{\circ}303$ (trigger 324362; De Pasquale et al. 2008; Barthelmy et al. 2008: see Figure 1). The data calibration and reduction were performed using the standard BAT analysis software distributed within FTOOLS under the HEASOFT package (version 6.9) and the latest CALDB release (2011 March 3). The mask-tagged (i.e., background-subtracted) counts of the source were extracted from the detector pixels illuminated by the source using the mask-weighting technique. The mask-weighting factors were calculated by BATMASKWTEVT using the ground-calculated position of Barthelmy et al. (2008, GCN 8215; right ascension[R.A.] = $40^{\circ}.101$, decl. = $61^{\circ}.210$, about 2.9 arcmin from the BAT onboard position reported by De Pasquale et al. 2008, GCN 8209; see Figure 2). Figure 3 shows the *Swift*/BAT image of the burst together with images of the same region obtained with different instruments, which are discussed below.

The mask-tagged light curves were created in the standard four energy bands, 15–25, 25–50, 50–100, and 100–350 keV (Figure 1) at 64-ms time resolution. The burst is visible in the first two bands (15–25 and 25–50 keV), while no significant

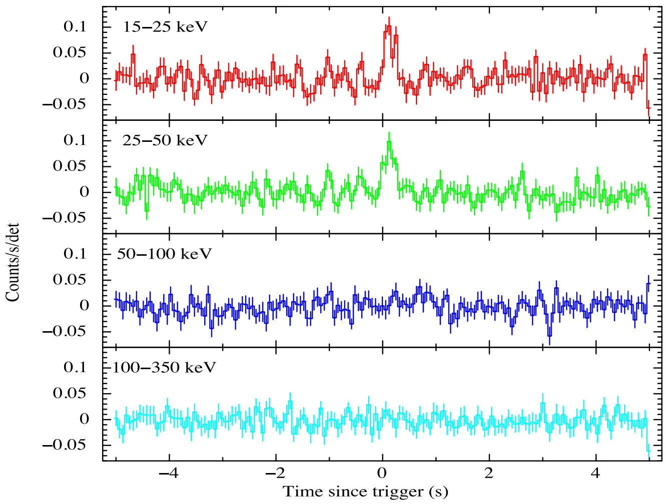

Figure 1. *Swift*/BAT light curves of the burst detected in the direction of LS I +61°303.

(A color version of this figure is available in the online journal.)

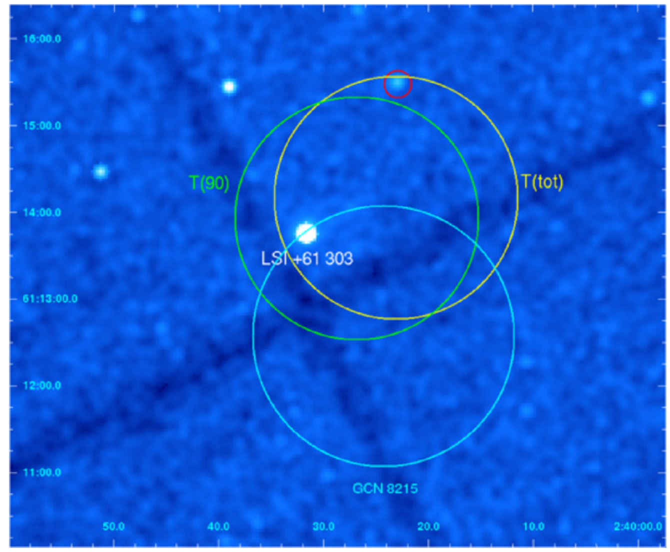

Figure 2. *Swift*/BAT positional error circles overimposed to the *Chandra* image of the field (smoothed with a Gaussian function with an FWHM of 3″). Cyan, green, and yellow circles report on the best position derived by Barthelmy et al. (2008) and our analysis using the T_{90} and the $T_{\rm tot}$ of the burst (see the text for details), respectively. The source within the red circle is the *Chandra* source discussed in Section 2.3.

(A color version of this figure is available in the online journal.)

excess is observed above 50 keV. The total duration of the event in the 15–50 keV band is $T_{\rm tot} \simeq 0.31$ s, while the T_{90} duration is 0.24 ± 0.05 s. These values were computed by the BATTBLOCKS task (based on the Bayesian Block algorithm; Scargle 1998) from a light curve with a 1 ms bin size.

We extracted a 15–50-keV sky image and performed a blind source detection over the T_{90} duration of the burst with the tool BATCELLDETECT. This script performs a least-squares fit of peaks in the map to the BAT point-spread function (a two-dimensional Gaussian) using the local rms noise to weight the pixels in the input map. A single, highly significant (11.0σ) point-like source was detected at the best-fit coordinates of R.A. = 40°.1119, decl. = +61°.2322 (essentially identical results were obtained using the total duration of the event: R.A. = 40°.0962, decl. = +61°.2362; signal-to-noise ratio (S/N) 11.0σ; see Figure 2).

The point-spread function fit using BATCELLDETECT also yields a formal uncertainty based on the least-squares covariance matrix. At 1σ this was 1.06 arcmin for the run using T_{90} (and 1.04 arcmin with $T_{\rm tot}$). However, because neighboring pixels in the coded mask images are inherently correlated, this error is known to be a poor estimator of the true uncertainty for high signal-to-noise detections. Therefore, we adopt a more conservative figure of 1.4 arcmin at 1σ (90%: 2.1 arcmin), which follows the prescriptions of the BAT calibration reports[5] and also includes a 0.25-arcmin systematic error (see Tueller et al. 2010). This position is consistent with that reported by Barthelmy et al. (2008; albeit that the center of the uncertainty visibly moves) and with that of LS I +61°303 (the angular separation being ~0.6 arcmin; see Figure 2). No source is detected in the BAT image, except for burst interval. The burst spectrum was extracted over the $T_{\rm tot}$ interval (we also extracted it from the T_{90} and found consistent results). The results of the spectral analysis are summarized in Table 1. To investigate the spectral evolution as a function of time, we computed a hardness ratio, but no spectral variations in the hardness ratio were visible.

Table 1
Spectral Analysis of the *Swift*/BAT Burst

Parameter	PL	BB	Brems
Γ	2.0 ± 0.3	...	...
kT (keV)	...	$7.5^{+0.9}_{-0.8}$	43^{+32}_{-14}
R (Km)	...	$0.27^{+0.07}_{-0.05}$	...
Flux	5 ± 2	4.5 ± 0.7	4.5 ± 0.9
Fluence	1.4 ± 0.6	1.4 ± 0.2	1.4 ± 0.3
χ^2/dof	1.29/14	1.07/14	1.22/14

Notes. *Swift*/BAT spectroscopy in the 15–50 keV energy range. Errors are at a 1σ confidence level for a single parameter of interest. Fluxes and fluences are in the 15–50 keV energy range and in units of 10^{-8} erg cm^{-2} s^{-1} and 10^{-8} erg cm^{-2}, respectively. The blackbody radius is calculated at infinity and for a distance of 2 kpc (which is the distance to LS I +61°303; Frail & Hjellming 1991).

2.2. *Analysis of the RXTE/HEXTE Observations: Can the Swift/BAT Short Burst Be the Result of the Spectral Evolution?*

The *RXTE*/PCA observation nearest to the *Swift*/BAT burst is located about 6 hr after the burst, with a total exposure time of 1492 s. We have analyzed this observation before, and no unusual behavior (and no flare) was found (see Ray et al. 2008; Torres et al. 2010).

To further investigate a possible connection between the short magnetar-like burst seen by *Swift*/BAT (see Section 2.1) and the typical ks-timescale bursts often observed in LS I +61°303 (Sidoli et al. 2006; Rea et al. 2010; Smith et al. 2009; Li et al. 2011), we searched for a possible hard X-ray counterpart to the ks-timescale flares observed by *RXTE*/PCA, taking advantage of the simultaneous observations performed by *RXTE*/HEXTE. We searched for any short/hard X-ray bursts that coincided with the longer flares observed in the 3–10-keV energy range (Li et al. 2011), assuming that a strong spectral softening might occur during the first seconds after the flare emission.

[5] See http://swift.gsfc.nasa.gov/docs/swift/analysis/bat_digest.html.

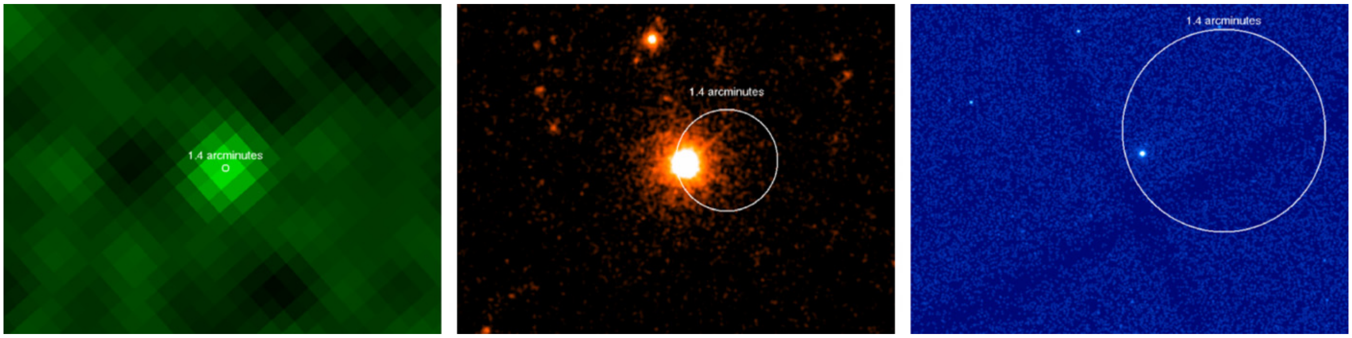

Figure 3. From left to right: the *Swift*/BAT image of the short burst (see Section 2.1) superimposing the spatial accuracy of our position determination (1′.4); the *Swift*–XRT image of all of the data collected so far on LS I +61°303 (165 ks), with the 1′.4 *Swift*/BAT error circle superimposed; and the *Chandra*/ACIS 50 ks image of the field of LS I +61°303 with the short burst positional accuracy overimposed.

(A color version of this figure is available in the online journal.)

The *RXTE*/HEXTE consists of eight detectors with a total area of about 1600 cm^2. The eight detectors are split up into two clusters of four detectors. During normal operation, each cluster is alternately pointed on and off of the source, generally every 16 or 32 s, to provide a nearly real-time background measurement. Here we use the HEXTE data covering the period between 2007 September and 2011 February. The data encompass 418 HEXTE pointed observations, providing a total exposure time of 621 ks on LS I +61°303.

In the light curve analysis of the HEXTE, we used "Standard Modes" data with a 16 s accumulation time, and we built the light curve in the 15–250 keV range. Data reduction was performed using the `HEASoft` tools, and the data were filtered using the standard HEXTE criteria. At the end of 2006, the first cluster (A) of detectors was fixed to always measure the source of interest, and no background measurements have been carried out since then. From 2009 December 13, cluster B was fixed to always measure the background, and no source detections are available with it. Additionally, Detector 2 (in the 0–3 numbering scheme) in the second cluster (B) started to function abnormally since 1996 March 6. Because of this, only Detectors 0, 1, and 3 in cluster B are used in our analysis until (but including) 2009 December 13. After that date, and as suggested by the *RXTE* team, we take data from cluster A as the source and data from cluster B as the background measurements. We select time intervals where the source elevation is $>10°$ and the pointing offset is $<0°.02$. The HEXTE light curves were generated, dead time corrected, and background subtracted using the REX script.

In the bottom panel of Figure 4, we show the 15–250-keV *RXTE*/HEXTE light curve of LS I +61°303 in 16 s time bins. For comparison in the top panel of Figure 4 we also show the 3–10 keV *RXTE*/PCA light curve of LS I +61°303 in 16 s time bins. Because of the addition of newer data, the latter enhances the results presented by Li et al. (2011). In particular, we discovered a sixth flare from the monitoring of PCA.[6]

As we explained above, since the overall HEXTE light curve is produced with different instruments at different

[6] The additional data set analyzed in this report covers the time span from 2010 September 5 to 2011 February 27 (MJD 55444–55619) and covers nearly another half year of data recently released on the HEASARC Web site. It includes 50 *RXTE* pointed observations identified by proposal numbers 95102 and 96102, providing a total exposure time of 70 ks on the source beyond what was reported by Li et al. (2011). We follow the exact same analysis chain as reported by Li et al. (2011) in analyzing the newest data. The general properties of the new sixth flare are very similar to those of the fourth flare reported by Li et al. (2011). Its power spectrum shows no evidence for the existence of any structure.

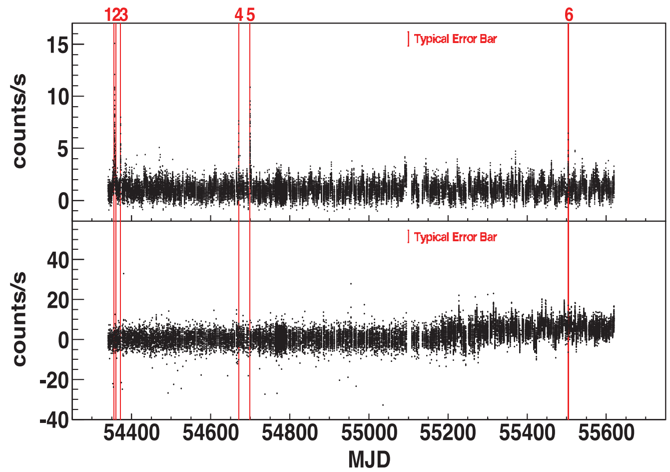

Figure 4. Top panel: The *RXTE*/PCA long-term light curve of LS I +61°303 in 3–10 keV. Bottom panel: The *RXTE*/HEXTE light curve in 15–250 keV. The highlighted regions are the five flares found in the PCA data (Li et al. 2011) plus a sixth additional one we uncovered as a result of continuous analysis of the new data.

(A color version of this figure is available in the online journal.)

times—cluster B as a source and a background before (and including) 2009 December 13 (MJD 55178), and cluster A as a source with cluster B as a background after that date—the average of the light curve changes, which is obvious in the bottom panel of Figure 4. Fitting a constant to the HEXTE light curve before MJD 55178 yields an average count rate of 0.11 ± 0.03 and a reduced $\chi^2 = 1.29$ (12915 degrees of freedom (dof)). Data accumulated for more than two years (2007 September–2009 December) generate a detection significance for LS I +61°303 of 4.4σ in the 15–250-keV band. The average count rate after MJD 55178 is 4.99 ± 0.03 and a fit to a constant yields a reduced $\chi^2 = 1.76$ (10745 dof).

To investigate whether there are possible flares in the *RXTE*/HEXTE, we looked at data points with a significance above 4σ over the average count rate. In the 15–250-keV band, 18 out of 23662 bin points have a significance large than 4σ. None of these corresponds to any of the flares detected by the PCA in the soft X-ray band, and we associate them with statistical fluctuations. A plot of the number of data points with a given count rate would show no deviation from a Gaussian fitting. Moreover, we divided the 15–250-keV energy band into 15–60 keV and 60–250 keV and found that all points above a 4σ significance in the larger energy range, 15–250 keV, are no

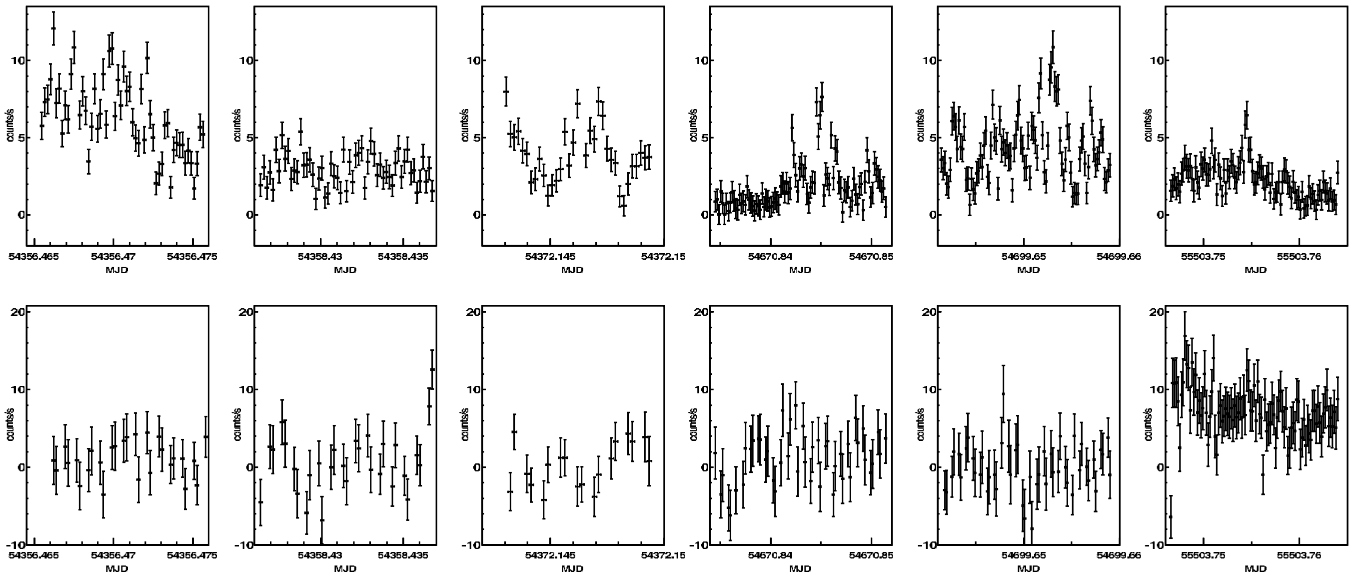

Figure 5. Light curve of the six flares in 3–10 keV (PCA) as observed at 15–250 keV by HEXTE. All of the light curves are binned at 16 s.

Table 2
The *RXTE*/HEXTE Counterparts to the Soft X-ray Flares

Flare	MJD	Average Count Rate	Significance	Reduced χ^2
1	54356	1.0 ± 0.5	0.3	17/26
2	54358	0.9 ± 0.5	0.2	64/28
3	54372	0	0	22/17
4	54670	1.0 ± 0.4	0.3	61/45
5	54699	0	0	43/47
6	55503	6.9 ± 0.3	0.5	133/94

Note. The average count rate, significance, and reduced χ^2 in the 15–250-keV energy band of the HEXTE data during the ks-timescale flares.

longer that significant in the 15–60-keV and/or the 60–250-keV ranges. Figure 5 corresponds to the six PCA flares marked in Figure 4, and it also shows a zoom view of the HEXTE light curve. The average count rate, significance, and reduced χ^2 of a constant fit to each flare are listed in Table 2, showing that all six PCA flares are not significantly detected in the 15–250-keV band.

If any of the PCA flares had been preceded by a similar burst to the one detected by the *Swift*/BAT, HEXTE would have seen them. To show this, we have simulated a burst observed by HEXTE with the *Swift*/BAT parameters. Using the HEXTE response, we found a significance of 4.64σ. If the *Swift*/BAT burst had been the result of the spectral evolution and related to the longer timescale flares usually detected from LS I $+61^{\circ}303$, then HEXTE would have spotted the flares in at least six of the instances in which we had simultaneous PCA and HEXTE coverage. This has not happened; the HEXTE has not seen any of the PCA ks-timescale flares, and we conclude that their nature is different from the *Swift*/BAT detection.

2.3. *Chandra/ACIS–I: Search for a Serendipitous Magnetar in the Field of LS I +61°303*

We analyzed an ~50-ks observation of LS I $+61^{\circ}303$ performed with the ACIS instrument (ObsID 10042) starting on 2006 April 7 22:08:59 (UT), in the "VERY FAINT" timed-exposure imaging mode (see also Paredes et al. 2007). The source was positioned in the back-illuminated ACIS–I3 CCD. Standard processing of the data was performed by the Chandra X-ray Center to Level 1 and Level 2 (processing software DS 8.0). The data were reprocessed using the CIAO software (version 4.1.2). We used the latest ACIS gain map and applied the time-dependent gain and charge transfer inefficiency corrections. The data were then filtered for bad event grades and only good time intervals were used. No high background events were detected. The final net exposure time was 49.105 ks.

We used the CIAO `celldetect` tool to search for sources by summing counts in square cells in the data set and comparing the counts to those of "background" cells. At each point where a cell is placed, an S/N of the source counts to the background counts is computed. We placed a detection limit of S/N = 4 and found only one source marginally compatible with the refined position of the *Swift*/BAT burst (see Section 2.1) at R.A. = 40°.095081, decl. = +61°.258468 (with a 1σ error of 1″.5 on the position), with a total of 0.3–10 keV counts of 50 ± 9 counts (see also Figure 2), translating into a count rate of 0.0010 ± 0.0002 counts s^{-1}. No radio, infrared, or optical counterparts have been detected for this source despite the deep archival observations covering this field of view (see Muñoz-Arjonilla et al. 2009; this source corresponds to their #12 of Table 3). Thus, we cannot formally exclude that the faint X-ray source detected by *Chandra* at the limit of the 1σ positional uncertainty of the burst (see Figure 2) might be the magnetar responsible for the short burst observed by *Swift*/BAT. Hence, independent from LS I $+61^{\circ}303$: assuming a thermal spectrum of ~0.3 keV, which is typical of a magnetar in quiescence (see Rea & Esposito 2011 for a review), and an absorption column density of 9×10^{21} cm^{-2} (relative to the whole Galactic value in the direction of the source, from the H I maps from Dickey & Lockman 1990), we derived a 0.3–10-keV observed flux of $\sim 6.1 \times 10^{-15}$ erg s^{-1} cm^{-2}. Assuming the source is located at the end of the Milky Way at a distance of 10 kpc, the corresponding luminosity would be $\sim 2.7 \times 10^{32}$ erg s^{-1}. This is consistent with it being a magnetar in quiescence. Given that there are only a few the TeV binaries, and only a few magnetars in the Galaxy have been detected by our experiments, the probability that both are seen at ~1′.4 from each other seems a priori low. A precise number cannot be computed without further assumptions at many levels (population distribution, total number of sources, etc.), which would probably make the results meaningless since we can never rule out a single random coincidence. Thus, the possibility is left open, although it does not seem to be the one that would be reasonably preferred.

3. THE *SWIFT*/BAT BURST IN THE CONTEXT OF MAGNETAR EMISSION

The properties of the burst observed by *Swift*/BAT (a very short duration and a thermal spectrum with a temperature of $\sim$7.5 keV; see Section 2.1) are typical of magnetars (see Aptekar et al. 2001; Woods & Thompson 2006; Mereghetti 2008), and they differ from other kinds of frequently observed flares such as type I bursts from X-ray binaries (which last $\sim$100 times longer) or gamma-ray bursts (which have harder spectra and are much more energetic). In particular, the burst flux (see Table 1) at a distance of 2.3 kpc (as for LS I $+61^\circ 303$) implies a 15–50-keV luminosity of $\sim 2 \times 10^{37}$ erg s^{-1}. The luminosity of this burst is on the lower end of the distribution of short bursts from magnetars, and it is in line with the bursts observed in the AXPs (see Gavriil et al. 2002; Woods et al. 2004), which are usually slightly less powerful (and last longer) than the bursts observed from the canonical SGRs (Gogus et al. 1999, 2001; Israel et al. 2008).

Perhaps the “relatively” low intensity of the single burst that has been found in decades of observations toward LS I $+61^\circ 303$ and in X-ray all-sky surveys suggests that the magnetic neutron star producing it has a magnetic field at the lower end of the typical magnetar regimes (hence around $\sim 5 \times 10^{13}$ G as is the case of PSR B1846$-$0258; Gavriil et al. 2008; Kumar & Safi-Harb 2008), or that it is a rather old magnetar (Myrs; see, e.g., Perna & Pons 2011). Note that in the first scenario a high rotational power can be present ($\dot{E} \sim 10^{35}$–10^{36} erg s^{-1}), while in the latter scenario the object would be a rather slow pulsar with very little energy stored in its rotation (see, e.g., Rea et al. 2010 for one such example).

However, in both cases the X-ray emission of LS I $+61^\circ 303$ may not be magnetar-like (e.g., due to resonant cyclotron scattering of a hot surface through a very dense magnetosphere; Thompson et al. 2002). In fact, a young magnetar with a relatively low B field and a high rotational power has an X-ray spectra dominated by non-thermal processes due to particle acceleration and shocks from its strong winds, while an old magnetar in quiescence is rather faint (10^{30}–10^{32} erg s^{-1}), having dissipated most of its magnetic energy, mostly thermally emitted from its surface. Thus, after considering the above and what we will explain in detail in the following sections, we believe that we might be witnessing a high-$\dot{E}$ magnetar with a magnetic field of the order of 10^{13}–10^{14} G in LS I $+61^\circ 303$.

4. MAGNETAR IN A BINARY SYSTEM

If we entertain the hypothesis that the origin of the magnetar-like event reported here could be LS I $+61^\circ 303$, an effort is in order to understand what the consequences are of the existence of a magnetar in this eccentric binary system. How will the observed multi-wavelength phenomenology be generated in such a case? The rest of this paper is devoted to analyzing this question.

4.1. *Physical Radii*

To begin considering these issues, we will introduce several radii (measured from the neutron star) that represent the relative strength of the system’s components and compare those with the position of the light cylinder, R_{lc} (see, e.g., Illarionov & Sunyaev 1975; Davies & Pringle 1981; Lipunov et al. 1994). The latter is

$$R_{lc} = \frac{cP}{2\pi} \simeq 4.77 \times 10^9 \left(\frac{P}{1\mathrm{s}}\right) \mathrm{cm}, \quad (1)$$

where P is the period of the pulsar, and we have adopted for it a scale of 1 s, which is typical of the observed magnetars. The Alfvén or magnetic radius, R_m, will be defined as the distance in which the magnetic field begins to dominate the dynamics of the infalling matter. Thus, it can be implicitly defined by the equality between the energy densities, which is attained at R_m,

$$\frac{B^2}{8\pi} = \frac{1}{2}\rho V_f^2. \quad (2)$$

Here, V_f is the free-fall velocity of the accreting matter onto the neutron star of mass M_{ns},

$$V_f = \sqrt{\frac{2GM_{ns}}{R}}; \quad (3)$$

B is the magnetic field in the inner magnetosphere, assumed to be of a dipole type with neutron star radius R_{ns}

$$B(R) = B_{ns}\left(\frac{R_{ns}}{R}\right)^3, \quad (4)$$

where R is measured from the neutron star center and ρ is the density of the accreting matter. The value of the latter is defined as

$$\rho = \frac{\dot{M}_{\mathrm{acc}}}{4\pi R^2 V_f}, \quad (5)$$

where $\dot{M}_{\mathrm{acc}}$ denotes the rate at which the matter is accreted—say at a distance r from the companion star—and can be obtained in the first approximation by using the Bondi–Hoyle–Littleton approach as (see, e.g., Bondi & Hoyle 1944)

$$\dot{M}_{\mathrm{acc}}(r) = \frac{1}{4}\dot{M}_*\left(\frac{R_{\mathrm{cap}}}{r}\right)^2. \quad (6)$$

In the latter formula, $\dot{M}_*$ denotes the stellar mass-loss rate (and, again, r is measured from the companion, not the neutron star). Finally, R_{cap} is the gravitational capture radius for a neutron star of mass M_{ns} as determined by the relative velocity of the neutron star with respect to the matter, V_{rel}, using the orbital and the stellar-wind velocity

$$R_{\mathrm{cap}} = \frac{2GM_{ns}}{V_{\mathrm{rel}}^2}. \quad (7)$$

4.2. *Regimes Under the Influence of a Polar Wind*

The stellar-wind velocity description is first assumed to have the typical form of a radiatively driven outflow from a high-mass star (e.g., Castor & Lamers 1979),

$$V_w = V_0 + (V_\infty - V_0)\left(1 - \frac{R_*}{r}\right)^\beta \simeq V_\infty\left(1 - \frac{R_*}{r}\right)^\beta, \quad (8)$$

where R_* is the stellar radius, $V_0 \sim 0.01 V_\infty$, $\beta \sim 1$, and $V_\infty \sim 1000$ km s^{-1} (Lamers & Cassinelli 1999). Note that in

Equation (8), r is measured from the companion; thus at R_m we will have $r(R_m) = d - R_m$, with d being the system separation. In an elliptic orbit of eccentricity e, the system separation is given by

$$d = a(1 - e\cos(\epsilon)), \tag{9}$$

where a is the semimajor axis and ϵ is the eccentric anomaly (see, e.g., Hilditch 2001). Considering that $d \gg R_m$, we neglect R_m in favor of d in the definition of $r(R_m)$ for subsequent calculations. We have checked, however, that not assuming this approximation would correct the results we achieve in a few percent, but it will significantly complicate the algebra. We also consider that the polar wind terminal velocity, V_∞, dominates the orbital speed (this is explicitly shown below). Taking this into account, the capture radius is given by

$$\begin{aligned} R_{\rm cap} &= \frac{2GM_{ns}}{V_w^2} \\ &= 3.73 \times 10^{10} \left(\frac{M_{ns}}{1.4\,M_\odot}\right)\left(\frac{V_\infty}{10^8\ \mathrm{cm\ s^{-1}}}\right)^{-2} \\ &\quad \times \left(1 - 0.69\left(\frac{R_*}{10\,R_\odot}\right)\left(\frac{a}{10^{12}\ \mathrm{cm}}\right)^{-1} \right. \\ &\quad \left. \times (1 - e\cos(\epsilon))^{-1}\right)^{-2\beta} \mathrm{cm}. \end{aligned} \tag{10}$$

We shall consider that a pulsar acts normally, i.e., it is rotationally powered and drives out a relativistic wind, if, at the capture radius, the pressure of the pulsar wind (cosmic rays and magnetic field), given in terms of its spin-down luminosity $L_{\rm sd}$ as

$$p_{\rm psr} = \frac{L_{\rm sd}}{4\pi R^2 c}, \tag{11}$$

exceeds the pressure of the stellar wind gas behind the shock ($p_w = \rho_w V_w^2$); see, e.g., Illarionov & Sunyaev (1975). In this case, the matter is swept away beyond $R_{\rm cap}$ and the system is the so-called ejector (Lipunov et al. 1994). The pressure condition can be written as

$$L_{\rm sd} > 4\pi R_{\rm cap}^2 c \rho_w V_w^2. \tag{12}$$

This adds a condition to the pulsar period (for other fixed magnitudes. For the pulsar to stop acting as an ejector, the period should be larger than

$$\begin{aligned} \left(\frac{P_{\rm out-ejector}}{1\ \mathrm{s}}\right) &> 3.09 \left(\frac{B}{10^{14}\ \mathrm{G}}\right)^{1/2} \left(\frac{\dot{M}_*}{10^{18}\ \mathrm{g\ s^{-1}}}\right)^{-1/4} \\ &\quad \times \left(\frac{V_\infty}{10^8\ \mathrm{cm\ s^{-1}}}\right)^{3/4} \left(\frac{a}{10^{12}\ \mathrm{cm}}\right)^{1/2} \\ &\quad \times \left(\frac{R_{ns}}{10^6\ \mathrm{cm}}\right)^{3/2} \left(\frac{M_{ns}}{1.4\,M_\odot}\right)^{-1/2} \\ &\quad \times (1 - e\cos(\epsilon))^{1/2} \\ &\quad \times \left(1 - 0.69\left(\frac{R_*}{10\,R_\odot}\right)\left(\frac{a}{10^{12}\ \mathrm{cm}}\right)^{-1} \right. \\ &\quad \left. \times (1 - e\cos(\epsilon))^{-1}\right)^{3\beta/4}. \end{aligned} \tag{13}$$

In these cases the pressure of the accreting matter with a decreasing radius ($R < R_{\rm cap}$) grows as $R^{-5/2}$, whereas $p_{\rm psr}$ grows as R^{-2}. Because of this, falling matter from $R_{\rm cap}$ begins, penetrating the light cylinder up to the point (if any) in which the quick rise of the dipolar magnetic field in the magnetosphere produces a pressure ($\propto R^{-6}$) able to stop it (i.e., at the Alfvén radius R_m). The pulsar no longer has a magnetosphere and can no longer generate a relativistic wind, so it is no longer in the ejector phase. To move out of this stage, and to ignite the normal (rotationally powered) pulsar again, an unscathed magnetosphere should be recovered. For this condition to happen, the period must be smaller than what is needed to have $R_m = R_{lc}$.

The value of R_m can be obtained using the previous expressions in Equation (2), as

$$\begin{aligned} R_m &= 2.1 \times 10^{10} \left(\frac{B}{10^{14}\ \mathrm{G}}\right)^{4/7} \left(\frac{\dot{M}_*}{10^{18}\ \mathrm{g\ s^{-1}}}\right)^{-2/7} \\ &\quad \times \left(\frac{V_\infty}{10^8\ \mathrm{cm\ s^{-1}}}\right)^{8/7} \left(\frac{a}{10^{12}\ \mathrm{cm}}\right)^{4/7} \\ &\quad \times \left(\frac{R_{ns}}{10^6\ \mathrm{cm}}\right)^{12/7} \left(\frac{M_{ns}}{1.4\,M_\odot}\right)^{-5/7} (1 - e\cos(\epsilon))^{4/7} \\ &\quad \times \left(1 - 0.69\left(\frac{R_*}{10\,R_\odot}\right)\left(\frac{a}{10^{12}\ \mathrm{cm}}\right)^{-1} \right. \\ &\quad \left. \times (1 - e\cos(\epsilon))^{-1}\right)^{8\beta/7} \mathrm{cm}. \end{aligned} \tag{14}$$

Although R_{lc} depends (linearly) on the spin period of the neutron star, R_m does not depend on P at all. Thus, the line $R_m = R_{lc}$ adds a condition to P. Neutron stars of sufficiently small periods have an unscathed magnetosphere even when they are in eccentric orbits with high mass-loss rate stellar companions, and thus behave as a normal pulsar. In general, to reignite the pulsar the condition over the period (considering all other magnitudes fixed) reads

$$\begin{aligned} \left(\frac{P_{\rm into-ejector}}{1\ \mathrm{s}}\right) &< 4.5 \left(\frac{B}{10^{14}\ \mathrm{G}}\right)^{4/7} \left(\frac{\dot{M}_*}{10^{18}\ \mathrm{g\ s^{-1}}}\right)^{-2/7} \\ &\quad \times \left(\frac{V_\infty}{10^8\ \mathrm{cm\ s^{-1}}}\right)^{8/7} \left(\frac{a}{10^{12}\ \mathrm{cm}}\right)^{4/7} \\ &\quad \times \left(\frac{R_{ns}}{10^6\ \mathrm{cm}}\right)^{12/7} \left(\frac{M_{ns}}{1.4\,M_\odot}\right)^{-5/7} \\ &\quad \times (1 - e\cos(\epsilon))^{4/7} \\ &\quad \times \left(1 - 0.69\left(\frac{R_*}{10\,R_\odot}\right)\left(\frac{a}{10^{12}\ \mathrm{cm}}\right)^{-1} \right. \\ &\quad \left. \times (1 - e\cos(\epsilon))^{-1}\right)^{8\beta/7}. \end{aligned} \tag{15}$$

Using the fiducial values in Equations (13) and (15), we see that a neutron star with a spin period usually measured for magnetars would be right at the transition range. Small changes in the mass-loss rate, for instance, can make the neutron star flip flop from accreting within the magnetosphere to behaving as a rotational powered pulsar.

To simplify the reasoning that follows, we will consider that the condition $R_m = R_{lc}$ not only establishes the *into-ejector* condition over the period P, but it also establishes the *out-of-ejector* regime. Indeed, the out-of-ejector condition obtained with Equation (13) is easier to fulfill (i.e., slightly smaller periods can fulfill it for equal values for the other magnitudes

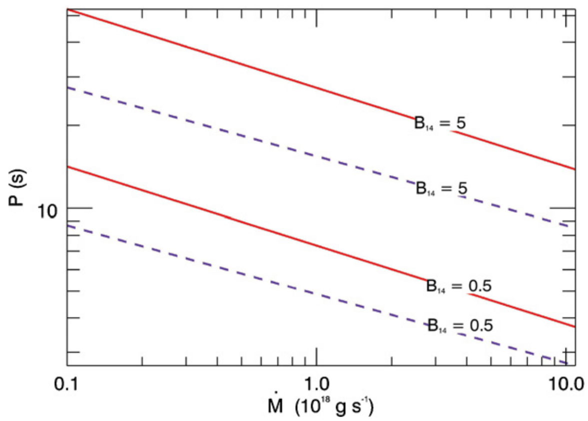

Figure 6. Comparison of the out-of-ejector conditions written in Equation (13)—in violet—and the constraint of the equality $R_m = R_{lc}$, given by Equation (15)—in red. The latter is always a more restrictive condition onto P, because equal values of the other magnitudes are involved. Two cases are shown for the surface magnetic fields of 5×10^{13} G and 5×10^{14} G. The eccentricity is assumed to be equal to zero and the LS I $+61°303$ semimajor axis is adopted in this example.

(A color version of this figure is available in the online journal.)

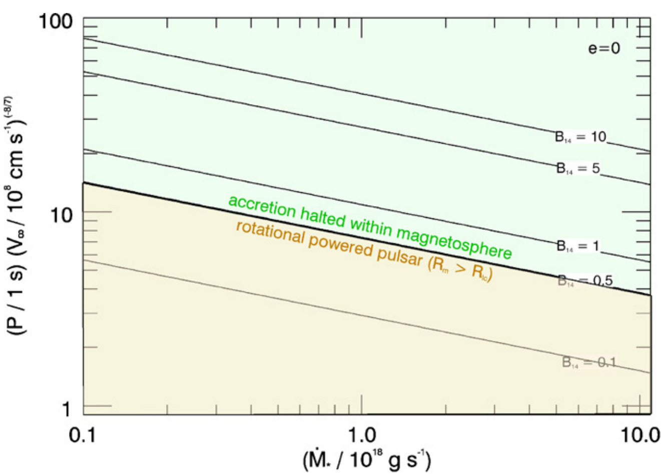

Figure 7. Phase space conditions for accretion regimes around a highly magnetic neutron star under the influence of a polar wind of terminal velocity V_∞ and mass-loss rate $\dot{M}_*$. It is assumed that the radius of the neutron star is 10^6 cm and its mass is 1.4 $M_\odot$. An example of the phase-space separation is marked for the case of the surface magnetic field of 5×10^{13} G. The eccentricity is assumed to be equal to zero and the LS I $+61°303$ semimajor axis is adopted in this example.

(A color version of this figure is available in the online journal.)

involved) than that obtained with Equation (15), whereas the shape of the constraint is similar. Figure 6 compares these two constraints over P, differing by a factor of ~1.57 from one another.

4.2.1. *Orbital Eccentricity Effects Under the Influence of a Polar Wind*

Figure 7 shows the condition $R_m = R_{lc}$ as given by Equation (15) for different values of the neutron star (surface) magnetic field. We adopt one order of magnitude up and one down for the possible variation in these parameters out of their fiducial values noted in Equation (15). We assume that the radius of the neutron star is 10^6 cm and its mass is 1.4 $M_\odot$. We adopt a semimajor axis value of 6×10^{12} cm and a radius of the massive star equal to 10 $R_\odot$, which are consistent with the measurements of the LS I $+61°303$ system (see, e.g., Casares et al. 2005; Grundstrom et al. 2007).

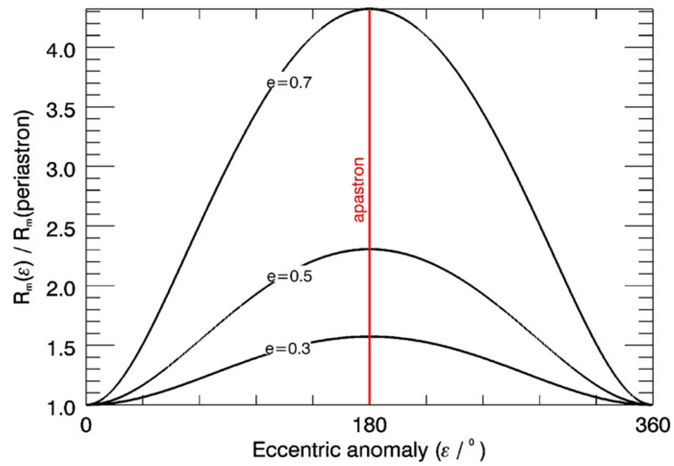

Figure 8. Ratio of the R_m-values along an eccentric orbit (under the influence of a polar wind of terminal velocity V_∞) with respect to that attained at the periastron, for a different eccentricity, as a function of the eccentric anomaly.

(A color version of this figure is available in the online journal.)

An example of the different physical behaviors of the system is noted in Figure 7 by the line $B = 5 \times 10^{13}$ G that separates the region of the plane for that specific value of the magnetic field where the accretion is halted within the magnetosphere (in light green, where $R_m < R_{lc}$) and from where the system acts as a rotationally powered system (in light yellow, where $R_m > R_{lc}$). This separation is valid at each of the possible (neutron star surface, dipolar) magnetic field strengths, which form a continuum throughout the plot.

As mentioned in the last section, Figure 7 and Equation (15) show that the observed values for the periods and magnetic fields of known magnetars together with fiducial (and commonly adopted) values of the stellar (polar) wind velocity and mass-loss rate of LS I $+61°303$ would make, assuming a circular orbit, $R_m \sim R_{lc}$. For example, a system hosting a pulsar with $P \sim 7$ s, where measured periods of magnetars cluster, and the fiducial values for the properties of the wind of the massive star, $V_w = 10^8$ cm s^{-1} and $\dot{M}_* \sim 10^{18}$ g s^{-1}, would be right at the line representing $R_m = R_{lc}$ for a surface magnetic field of $B = 5 \times 10^{13}$ G.

However, we must take into account that the orbit of LS I $+61°303$ is not circular, and its eccentricity has been quoted in the range of 0.55–0.72 (see, e.g., Casares et al. 2005; Grundstrom et al. 2007; Aragona et al. 2009). R_m then becomes a function of the orbital position, and it can be represented as a function of the system's eccentric anomaly for a given value of eccentricity. Figure 8 shows the ratio of the R_m values along an eccentric orbit with those attained by R_m at the periastron. For the quoted eccentricity, R_m is a factor of between two and four smaller at the periastron than what it is at the apastron. Then, if the magnetar-composed system fulfills the condition $R_m > R_{lc}$ at the apastron and the inner magnetosphere behaves as a rotational powered pulsar, it will likely fulfill $R_m < R_{lc}$ at the periastron. This is graphically shown in Figure 9, which shows, for $e = 0.6$, the region of the phase space in which a magnetar hosted in LS I $+61°303$ would change behavior. Under the assumption of a dominant polar wind the fiducial values of all of the parameters would position the system right in the middle of the flip-flop regime, with the putative magnetar in LS I $+61°303$ acting as a rotationally powered system in the apastron (R_m is larger than the light cylinder in the apastron), and accreting within the magnetosphere in the periastron

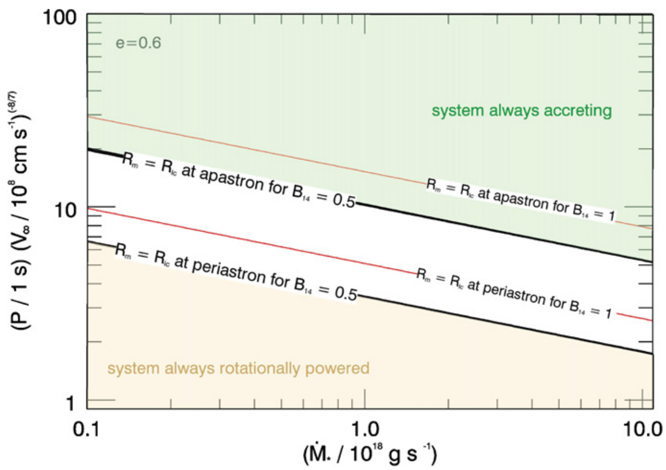

Figure 9. Examples of the region of the phase space for a system similar to LS I $+61^\circ303$ where the system would change behavior from accreting within the magnetosphere (in the periastron) to be a rotationally powered pulsar (in the apastron). Each of these phase-space regions producing this flip-flopping behavior is located within the two lines corresponding to an equal magnetic field label; several pairs are shown. An example with $B = 5 \times 10^{13}$ G is explicitly depicted (the central white region of the plot is the flip-flopping area; the top green part corresponds to the always-accreting systems, and the bottom light-yellow part corresponds to neutron stars that are always acting as a rotationally powered pulsar along the orbit). The flip-flopping region moves up in the plot for higher magnetic fields (an example with $B = 10^{14}$ G is shown with red lines). The neutron star is assumed to be subject to the influence of a polar wind of terminal velocity V_∞.

(A color version of this figure is available in the online journal.)

(R_m is smaller than the light cylinder in the periastron). For the usual magnetar parameters, this is the natural solution for the LS I $+61^\circ303$ behavior along its orbit.

4.2.2. *Kind of Accretion Under the Influence of a Polar Wind*

To further consider the possible accretion scenario, we will define two additional radii. Let us consider first the rotational velocity of the magnetosphere at the position R_m, which is given by

$$V_{\rm rot} = \frac{2\pi R_m}{P}, \tag{16}$$

and the Keplerian velocity of the infalling matter, which is instead given by

$$V_{\rm Kep} = \sqrt{\frac{GM_{ns}}{R_m}}. \tag{17}$$

These two velocities allow for the definition of the co-rotation radius, $R_{\rm cor}$, when $V_{\rm Kep} = V_{\rm rot}$, which can be written as

$$R_{\rm cor} = \left(\frac{GM_{ns}P^2}{4\pi^2}\right)^{1/3} = 1.67 \times 10^8 \left(\frac{M_{ns}}{1.4\,M_\odot}\right)^{1/3} \left(\frac{P}{1\ \rm s}\right)^{2/3} \rm cm. \tag{18}$$

The co-rotation radius represents the position of the centrifugal barrier for the infalling material created by the neutron star rotation. $R_m > R_{\rm cor}$ when

$$\left(\frac{P}{1\ \rm s}\right) < 1456.3 \left(\frac{B}{10^{14}\ \rm G}\right)^{6/7} \left(\frac{\dot{M}_*}{10^{18}\ \rm g\ s^{-1}}\right)^{-3/7} \times \left(\frac{V_\infty}{10^8\ \rm cm\ s^{-1}}\right)^{12/7} \left(\frac{a}{10^{12}\ \rm cm}\right)^{6/7} \left(\frac{R_{ns}}{10^6\ \rm cm}\right)^{18/7} \times \left(\frac{M_{ns}}{1.4\,M_\odot}\right)^{-37/14} (1 - e\cos(\epsilon))^{6/7} \times \left(1 - 0.69\left(\frac{R_*}{10\,R_\odot}\right)\left(\frac{a}{10^{12}\ \rm cm}\right)^{-1} \times (1 - e\cos(\epsilon))^{-1}\right)^{12\beta/7}. \tag{19}$$

Unless the values far off from the fiducial ones are invoked, the inequality in Equation (19) is always respected. In particular, when the period is such that R_m is less, but of the same order as R_{lc}, the system halts accretion at distances from the neutron star, which always results in super-Keplerian velocities.

When the accretion is halted in the magnetosphere, i.e., $R_m < R_{lc}$, at a position that is super-Keplerian, $R_m > R_{\rm cor}$, the system can be in either the magnetic inhibition regime when $R_{\rm cap} < R_m$ or in the stage of a supersonic propeller when $R_{\rm cap} > R_m$ (see, e.g., Bozzo et al. 2008). To decide between these latter possibilities it is useful to consider the relative extent of $R_{\rm cap}$ with respect to R_{lc}. Indeed, when we already know that the matter proceeds within the magnetosphere, i.e., $R_m < R_{lc}$, if $R_{lc} < R_{\rm cap}$, we also know that $R_m < R_{\rm cap}$, and the system behaves as a supersonic propeller. The inequality $R_{lc} < R_{\rm cap}$ happens when the period of the neutron star fulfills the following relation:

$$\left(\frac{P}{1\ \rm s}\right) < 7.87 \left(\frac{V_\infty}{10^8\ \rm cm\ s^{-1}}\right)^{-2} \left(\frac{M_{ns}}{1.4\,M_\odot}\right) \times \left(1 - 0.69\left(\frac{R_*}{10\,R_\odot}\right)\left(\frac{a}{10^{12}\ \rm cm}\right)^{-1} \times (1 - e\cos(\epsilon))^{-1}\right)^{-2\beta}. \tag{20}$$

In general, though, $R_{\rm cap} > R_m$ implies, e.g., a condition on the stellar wind velocity as a function of the other parameters in phase space,

$$\left(\frac{V_\infty}{10^8\ \rm cm\ s^{-1}}\right) < 1.2 \left(\frac{B}{10^{14}\ \rm G}\right)^{-2/11} \left(\frac{\dot{M}_*}{10^{18}\ \rm g\ s^{-1}}\right)^{1/11} \times \left(\frac{a}{10^{12}\ \rm cm}\right)^{-2/11} \left(\frac{R_{ns}}{10^6\ \rm cm}\right)^{-6/11} \times \left(\frac{M_{ns}}{1.4\,M_\odot}\right)^{6/11} (1 - e\cos(\epsilon))^{-2/11} \times \left(1 - 0.69\left(\frac{R_*}{10\,R_\odot}\right)\left(\frac{a}{10^{12}\ \rm cm}\right)^{-1} \times (1 - e\cos(\epsilon))^{-1}\right)^{-\beta}. \tag{21}$$

Figure 10 shows the condition on V_∞ for different values of the phase-space parameters and for a circular orbit (zero eccentricity). Several examples are noted (for different values of the magnetic field) and are represented by the solid lines. Each of these lines separates the behavior of the system from being a propeller (below it) to being magnetically inhibited (above it). We particularly note this division for $B = 5 \times 10^{13}$ G. Again, the eccentricity value of the orbit is important. Figure 11 shows the ratio of the maximal V_∞ value below which the system is a propeller for a given eccentricity, with respect to the value it attains in a circular orbit. For instance, for $e = 0.6$, the

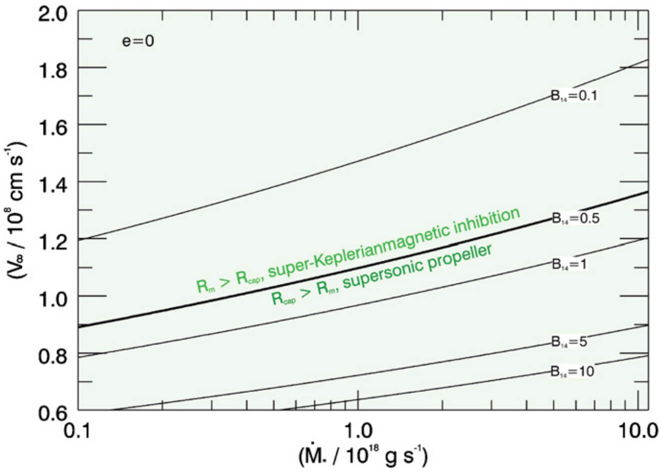

Figure 10. Phase-space conditions for the accretion regimes around a highly magnetic neutron star. Above each of the curves, which correspond to the different values of the magnetic field (an example is given for $B = 5 \times 10^{13}$ G), the system is a super-Keplerian magnetic inhibitor. Below that line, the system acts as a supersonic propeller. The eccentricity of the orbit is assumed to be zero in this plot. The light-green shadow depicts the fact that the system halts matter within the magnetosphere in the whole of the phase space.

(A color version of this figure is available in the online journal.)

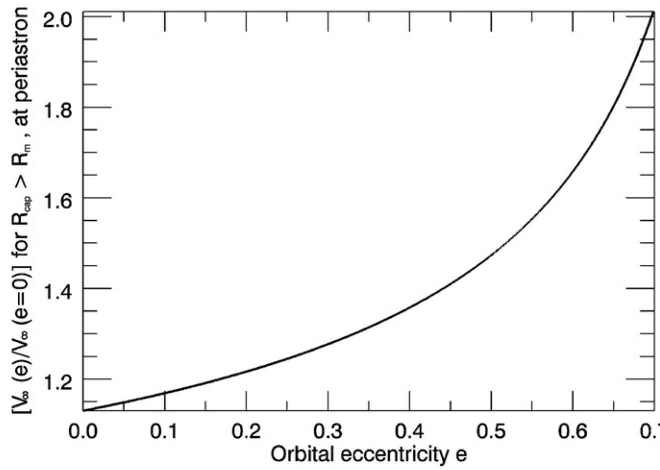

Figure 11. Ratio of the maximal V_∞ value below which the system is a propeller for a given eccentricity, with respect to the needed value in a circular orbit. The higher the eccentricity, the larger the value of V_∞ that can accommodate a propeller behavior for a highly magnetic neutron star.

limiting velocity is enlarged by a factor of 1.65, meaning that each of the curves in Figure 10 should be displaced in the y-axis by this factor. For the noted example with $B = 5 \times 10^{13}$ G and the fiducial value of $\dot{M}_* = 10^{18}$ g s^{-1}, all systems with $V_\infty \simeq 2 \times 10^8$ cm s^{-1} or less are supersonic propellers.

4.3. Describing an Equatorial Disk Outflow and Its Caveats

We will now consider a situation in which a neutron star feels the influence of an equatorial disk outflow, where the matter is moving with the velocity vector $\bar{V}_{w,eq}$. The uncertainties in describing the equatorial disk have a much more pronounced impact on the derivations. This section intends to give some of the details about this, and, if nothing else, to make the caveats in the usual assumptions of analytical treatments more explicit.

4.3.1. A Bondi–Hoyle Approach and Its Problems

We start by coming back to Equation (7) for the $R_{\rm cap}$ definition and the first study, which are the components in this scenario that give rise to the value of $V_{\rm rel}$. Once $V_{\rm rel}$ is determined, most of the (analytical) literature on this topic continues to assume that the accretion rate is given by

$$\dot{M}_{\rm acc} = \pi \frac{(2GM_{ns})^2}{V_{\rm rel}^3} \rho_{eq} = \pi R_{\rm cap}^2 V_{\rm rel} \rho_{eq}, \tag{22}$$

where ρ_{eq} is obtained from the continuity equation for radially outflowing matter, with velocity $V_{eq,r}$, a disk of a half-opening angle Θ,

$$\dot{M}_*^{eq} = 4\pi r^2 \sin(\Theta)\, V_{eq,r}\, \rho_{eq}, \tag{23}$$

and where $\dot{M}_*^{eq}$ is the mass-loss rate in this outflow. These equations already imply that the Bondi–Hoyle approximation is valid for the accretion process onto the star resulting from the equatorial disk outflow, i.e., that the material entering a cylinder of the radius equal to the accretion radius will be captured. This may not be true for several reasons. First, even when the Bondi–Hoyle is assumed, the accretion radius can exceed the vertical size of the disk, and, if so, the real accreted mass should be smaller (see, e.g., Zamanov 1995; Zamanov et al. 2001, and the discussion below). Also, short-lived Roche–Lobe overflows can occur in close binaries. This approximation also assumes that the Be disk is not affected in any way by the passage of the compact object, which is wrong based on the simulations by Okazaki et al. (2002). In general, Be disks in binaries are tidally truncated (Okazaki & Negueruela 2001) and, because of this, it is very hard to estimate the accretion rate onto the compact companion without running numerical simulations (see, e.g., Okazaki et al. 2002 and Romero et al. 2007).

Nevertheless, it is instructive to see how large of an accretion rate is possible by using the Bondi–Hoyle approximation, and, particularly, how sensitive it is to changes in the assumptions. With regard to the other components of $V_{\rm rel}$, apart from those contained in $\bar{V}_{w,eq}$, the orbital velocity of the neutron star around the star is given by Kepler's law

$$V_{\rm orb} = \sqrt{\frac{GM_*^3}{(M_* + M_{ns})^2}\left(\frac{2}{d} - \frac{1}{a}\right)}, \tag{24}$$

where M_* is the mass of the stellar companion and the remaining magnitudes have been already defined. In terms of the true anomaly θ, which is defined with the convention of having $\theta = 0$ at the periastron, we can write

$$d = \frac{a(1 - e^2)}{1 + e\cos(\theta)}, \tag{25}$$

for the neutron star—Be star separation. As we will see, the magnitudes for the forthcoming assumptions for the equatorial wind velocity make $V_{\rm orb}$ no longer negligible with respect to the other components of $V_{\rm rel}$. We have already assumed that the equatorial disk matter will move with a radial, $V_{eq,r}$ velocity. In addition, it may have an azimuthal, $V_{eq,\phi}$, component—which is assumed to be positive for the rotation in the direction of the orbital motion—such that $V_{w,eq}^2 = V_{eq,r}^2 + V_{eq,\phi}^2$. Once these are defined, the relative velocity is given by $\bar{V}_{\rm rel} = \bar{V}_{w,eq} - \bar{V}_{\rm orb}$. Its magnitude is given by

$$V_{\rm rel}^2 = V_{\rm orb}^2 + V_{eq,\phi}^2 + V_{eq,r}^2 - 2V_{\rm orb}V_{eq,\phi}\cos(\phi) - 2V_{\rm orb}V_{eq,r}\sin(\phi), \tag{26}$$

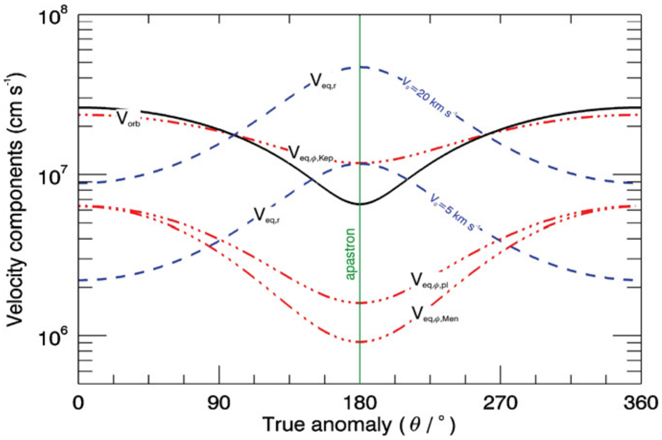

Figure 12. Components of the velocity vectors that were considered. Alternatives for the assumption of the circular velocity of the wind matter are plotted in red (three-dot dashed). A couple of radial velocity components with a different pre-factor are plotted in blue (dashed). The orbital speed of the neutron star is depicted by the solid black line.

(A color version of this figure is available in the online journal.)

where ϕ is the flight-path angle between the neutron-star velocity and the local horizon and measured from the latter to the neutron-star velocity vector. The flight-path angle is positive when the neutron star is traveling from the periastron to the apastron and negative vice versa.

To proceed further, we need to define the functional form adopted for $V_{eq,r}$ and $V_{eq,\phi}$. However, the magnitude of those is far from clear, as is also the case, for instance, for the termination distance of the equatorial wind or its granularity. In this exploratory section, we can only base our study on different analytical formulations that have already been used in the literature to represent these components. The first obvious assumption is to consider that there is no azimuthal movement in the matter of the equatorial disk, $V_{eq,\phi,0} = 0$ (e.g., Zamanov et al. 2001; Gregory & Neish 2002). Gregory & Neish (2002) considered several other parameterizations for $V_{eq,\phi}$ that go from a Keplerian velocity $V_{eq,\phi,\mathrm{Kep}} = \sqrt{GM_*/r}$, which would be the natural choice for a viscous decretion disk, to different power laws assumed for the rotation of the envelope $V_{eq,\phi,\mathrm{Men}} = V_*(r/R_*)^{-1.4}$ (see also Mennickent et al. 1994), where V_* is the stellar rotation velocity—set to 360 km s^{-1} or $V_{eq,\phi,\mathrm{pl}} = V_{0,\phi}(R_*/r)/\sin(i)$ with i being the inclination and $V_{0,\phi} \sim 1$ km s^{-1} (see Casares et al. 2005 and Bosch-Ramon et al. 2006). As is seen in Figure 12, these latter alternatives produce similar values (within an order of magnitude) for the magnitude of the azimuthal velocity component along the orbit, and all of them are also similar to the orbital speed.

To define the radial velocity component one can also assume, to the first approximation, that it is close to zero. The outflow velocities are so low that typically only upper limits (of the order of 1 km s^{-1}) are observationally obtained (Okazaki 2010). Marlborough et al. (1997) used, for instance, $V_0 = 0.3$ km s^{-1} for their disk parameters. One could also adopt the power-law wind density $\rho_{eq} \propto r^{-n}$, with $n = 3.2$, used by Waters (1986) and Martí & Paredes (1995) in fitting their near-infrared data. For a constant outflow rate, the continuity equation leads to a radial outflow of the form $V_{eq,r} = V_0(r/R_s)^{n-2}$, where again r is the distance measured from the companion star and V_0 is quoted from a few to a few tens of km s^{-1}. V_0 was assumed as 5 km s^{-1} in Waters (1986) and in the range of 2–20 km s^{-1} in Martí & Paredes (1995); this fixes the density of the equatorial wind matter at the star surface on the order of 10^{-11} g cm^{-3}, with a half-opening angle $\Theta = 15°$. Gregory & Neish (2002) obtain the radial velocity starting from the azimuthal velocity, forcing the accreted mass to be related to the radio emission along the orbit. For distances smaller than 10 R_s, the radial velocities obtained in this manner are quite similar to the functional form assumed above (see Figure 5 in Gregory & Neish's paper). In addition, we take into account that the differences beyond this distance will not play a relevant role if the disk truncates what is modeled with a phenomenological cut to the density of the equatorial wind beyond a distance of $\sim$10 R_* (see, e.g., Gregory & Neish 2002; Bosch-Ramon et al. 2006). By assuming a cut at $\sim$12 R_* the second accretion peak seen in some of the curves below is also preserved.

In Figure 13 we plot V_{rel} as a function of the orbital phase—defined in terms of the eccentric anomaly as $\phi_p = (\epsilon - e\sin(\epsilon))/(2\pi)$, so that the phase is equal to zero at the periastron—for the alternative descriptions of the previously considered outflow. In particular, we see that large differences appear along the orbital phases of the LS I +61°303 system for the Keplerian, Mennickent, and power-law descriptions of the azimuthal velocity. For the latter case, this plot also shows how large the influence is of a changing initial velocity in $V_{eq,r}$ from 3 to 5 km s^{-1} along the whole orbit. For completeness we also show the case of zero azimuthal velocity (the case of zero radial velocity would produce a similar curve to the Keplerian case, particularly at low phases, which is depicted in red in the figure). The accretion rate is very sensitive to small changes in V_{rel}.

Figure 13 also shows the accretion rate onto the neutron star, which was obtained via Equation (23), for a few of the cases. The solid lines depict the results that correspond to the non-dissolving equatorial disk; the dashed lines correspond to those where the disk density has been cut off beyond 10 R_s. The two blue lines correspond to the result with an initial radial velocity of 3 (top curve) and 5 km s^{-1} (bottom curve), respectively. The horizontal line depicts the assumed stellar mass-loss rate ($1.3 \times 10^{-7}\ M_\odot$ yr^{-1}), which is consistent with the equatorial disk density at the surface being $\sim 1 \times 10^{-11}$ g cm^{-3}. The fact that some of the curves are atop the horizontal line in Figure 13 must be understood as an unphysical effect produced by the Bondi–Hoyle formula. This situation was also found earlier (see, e.g., Zamanov 1995; Martí & Paredes 1995; Bosch-Ramon et al. 2006; Orellana & Romero 2007, etc.), although the plotting of the ratio of the accretion rate with respect to the value it attains at the periastron may make this fact less clear at first sight. The failure of the Bondi–Hoyle formula has been treated differently by different authors, either by ignoring it, given the approximate character of the studies (see above-quoted references), to the addition of one or several ad hoc cuts (Zamanov et al. 2001), or by the use of radio data to rescale it. In the last case, Gregory & Neish (2002) assumed that the accretion-rate value should be corrected by making $S(r) = K(r)\dot{M}_{\mathrm{acc}}$, where $S(r)$ is the radio flux density (as measured along the orbit at, e.g., 8.3 GHz) and $K(r)$ is the factor of proportionality, depending on the object's separation or orbital phase. The former expression can be rewritten as $k(r)\rho(r) = S(r)V_{\mathrm{rel}}^3$, where $k(r) = K(r)\pi(2GM)^2$. If V_{rel} is computed, $S(r)$ is taken from the data, and $\rho(r)$ is assumed equal to $\rho_{eq} \propto r^{-n}$ as above. $k(r)$ can be derived and $K(r)$ immediately follows (Gregory & Neish 2002; see their Figure 6). From this approach all values of the accretion rate are significantly diminished, and they correspond to the range of 0.001–0.01 Eddingtons, which is equivalent to a reduction of >100 times

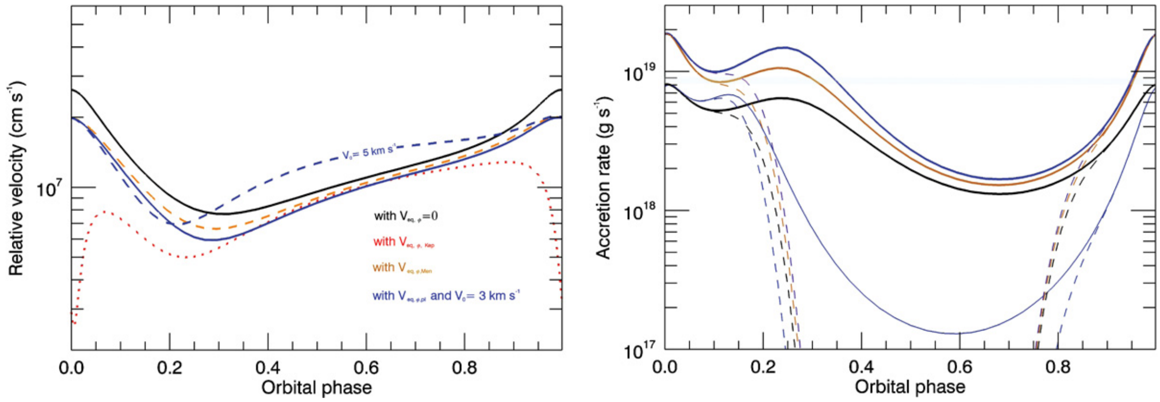

Figure 13. Left panel: relative velocity along the LS I $+61°303$ orbit (phase zero is the system's periastron) for different alternatives for the description of the equatorial wind outflow. No density cut is assumed in this plot. The blue lines correspond to assuming $V_{eq,\phi,\mathrm{pl}} = 1.17 \times 10^7((R_*/r)/\sin(i))$ cm s^{-1} for different assumptions of the V_0 factor in $V_{eq,r}$. Right panel: accretion rate on to the neutron star that was obtained by means of the Bondi–Hoyle formulation for different relative velocities. The color coding follows Figure 13; see the text for details.

(A color version of this figure is available in the online journal.)

the value of the accretion rate at the periastron. This order of magnitude for the accretion rate would be consistent with the one numerically obtained by Romero et al. (2007). As noted by Orellana et al. (2007; see their Figure 1), some of the accretion rate curves of Figure 13 display similar features, e.g., the position of the local maxima in phase, with the one numerically obtained, but there are approximately three orders of magnitude of difference in the absolute value. We note that Romanova et al. (2003) and Toropin et al. (2006) consistently found that the fraction of the Bondi accretion rate that accretes to the surface of the star, which is obtained from magnetohydrodynamics (MHD) simulations of the accretion to a rotating star in the propeller regime, is much less than Bondi's. These simulations will be discussed further.

4.3.2. Regimes and Orbital Eccentricity Effects Under the Influence of an Equatorial Disk Outflow

The analysis in the previous section emphasizes that the problem of matter exchange in an equatorial wind setting is hard to quantify in an analytical treatment. It can be likely only assessed via numerical simulations; however, these do not lack their own complexity and caveats (see, e.g., Zdziarski et al. 2010 and Okazaki et al. 2011 for an assessment). Nevertheless, the previous discussion is enough to note that at periastron distances, and even considering a significant reduction of the accretion rate shown in Figure 13, if the neutron star passes through the disk it is likely that the accretion from the equatorial outflow dominates over that from the polar wind, implying that $\dot{M}_{\mathrm{acc},eq} > \dot{M}_{\mathrm{acc,polar}}$. For comparison, we recall that the polar outflow accretion, which is computed by using Equations (6) and (10), leads to values that are maximal at the periastron, where it attains $\sim 2 \times 10^{14}$ g s^{-1} (this value is two orders of magnitude less than the expected equatorial-outflow accreted-matter resulting from the numerical simulations) then quickly falls to 5×10^{12} g s^{-1}. In this situation, it is even easier for a magnetar to allow matter to enter into its magnetosphere, given that R_m is smaller under the equatorial wind influence. Indeed,

$$R_m = 8.2 \times 10^9 \left(\frac{B}{10^{14}\ \mathrm{G}}\right)^{4/7} \left(\frac{\dot{M}_{\mathrm{acc},eq}}{10^{16}\ \mathrm{g\ s^{-1}}}\right)^{-2/7} \times \left(\frac{M_{ns}}{1.4\, M_\odot}\right)^{-1/7} \left(\frac{R_{ns}}{10^6\ \mathrm{cm}}\right)^{12/7} \mathrm{cm}. \qquad (27)$$

For matter in this outflow to enter within the magnetosphere,

$$\left(\frac{P}{1\ \mathrm{s}}\right) > 1.7 \left(\frac{B}{10^{14}\ \mathrm{G}}\right)^{4/7} \left(\frac{\dot{M}_{\mathrm{acc},eq}}{10^{16}\ \mathrm{g\ s^{-1}}}\right)^{-2/7} \times \left(\frac{M_{ns}}{1.4\, M_\odot}\right)^{-1/7} \left(\frac{R_{ns}}{10^6\ \mathrm{cm}}\right)^{12/7}. \qquad (28)$$

The larger the accretion rate at the periastron, the easier it is for pulsars with lower periods to have matter within the magnetosphere. For fiducial values this is reflected by comparing Equations (28) and (15).

Additionally, using Equations (18) and (27) to ask for the inequality $R_m > R_{\mathrm{cor}}$ to be fulfilled implies a condition over the period

$$\left(\frac{P}{1\ \mathrm{s}}\right) < 344 \left(\frac{B}{10^{14}\ \mathrm{G}}\right)^{6/7} \left(\frac{\dot{M}_{\mathrm{acc},eq}}{10^{16}\ \mathrm{g\ s^{-1}}}\right)^{-3/7} \times \left(\frac{M_{ns}}{1.4\, M_\odot}\right)^{-5/7} \left(\frac{R_{ns}}{10^6\ \mathrm{cm}}\right)^{18/7}, \qquad (29)$$

which is easy to satisfy for all of the measured values of P for the magnetars. Finally, using the definition of R_{cap}, the condition $R_{\mathrm{cap}} > R_m$ implies

$$\left(\frac{B}{10^{14}\ \mathrm{G}}\right) < 14.1 \left(\frac{\dot{M}_{\mathrm{acc},eq}}{10^{16}\ \mathrm{g\ s^{-1}}}\right)^{1/2} \left(\frac{V_{\mathrm{rel}}}{10^8 \mathrm{cm\,s^{-1}}}\right)^{-7/2} \times \left(\frac{M_{ns}}{1.4\, M_\odot}\right)^{2} \left(\frac{R_{ns}}{10^6\ \mathrm{cm}}\right)^{-3}. \qquad (30)$$

We lack accurate knowledge of V_{rel} to assess the former inequality, other than observing that the fiducial value chosen is—to be conservative—one order of magnitude larger than the one shown in Figure 13. A smaller value for V_{rel} (smaller than the one chosen as fiducial) would make the inequality even easier to fulfill. Then, this condition is not restrictive for magnetars. This implies that, under the influence of an equatorial outflow with an accretion rate on the order of 10^{15-16} g s^{-1}, and with the caveat of not having a precise description of the short-lived effects, such as a Roche–Lobe overflow or a formation of a transient accretion disk, the system would also act as a propeller in its periastron.

5. ENERGETICS

5.1. Maximal Energy of Electrons at Periastron Shocks

To analyze the possible maximal electron acceleration in the propeller we consider, e.g., Bednarek (2009), the rate of energy increase and of energy losses in a shock formed at the magnetic radius position, which is where turbulent motion of a strongly magnetized medium is considered to be prone to particle acceleration. The acceleration gain can be parameterized as

$$\left(\frac{dE}{dt}\right)_{\rm acc} = \zeta c E / R_L = \zeta c e B, \tag{31}$$

where ζ is an efficiency of acceleration (the fiducial value is 10%), R_L is the Larmor's radius, and e is the electron charge. B is the magnetic field, and its value will be obtained from Equation (4). ζ is a free parameter here and the fiducial value for it has been chosen conservatively; generally $\zeta \ll 1$, and it is close to 1 only in extreme accelerators (e.g., Aharonian et al. 2002; Khangulyan et al. 2007, 2008, considered values of $\zeta \sim 10^{-2}$–10^{-4}).

Given that the electrons of the highest energies lose energy mostly via the synchrotron process,

$$\left(\frac{dE}{dt}\right)_{\rm loss} = \frac{4}{3} c \sigma_T \rho_B \gamma^2. \tag{32}$$

Here, σ_T is the Thompson cross section, γ is the electron Lorentz factor, and $\rho_B = B^2/8\pi$ is the energy density of the magnetic field. The maximum energy of the electrons is determined by the balance of the two former equations, which, by means of Equation (14), results in

$$\begin{aligned}\gamma_{\rm max}^{\rm (polar)} = 1.1 \times 10^7 \left(\frac{\zeta}{0.1}\right)^{1/2} \left(\frac{B}{10^{14}\ {\rm G}}\right)^{5/14} \\ \times \left(\frac{\dot{M}_*}{10^{18}\ {\rm g\ s^{-1}}}\right)^{-3/7} \left(\frac{V_\infty}{10^8\ {\rm cm\ s^{-1}}}\right)^{12/7} \\ \times \left(\frac{a}{10^{12}\ {\rm cm}}\right)^{6/7} \left(\frac{R_{ns}}{10^6\ {\rm cm}}\right)^{15/14} \\ \times \left(\frac{M_{ns}}{1.4\, M_\odot}\right)^{-15/14} (f(e))^{3/2},\end{aligned} \tag{33}$$

where

$$\begin{aligned}f(e) = (1 - e\cos(\epsilon))^{4/7} \\ \times \left(1 - 0.69 \left(\frac{R_*}{10\, R_\odot}\right) \left(\frac{a}{10^{12}\ {\rm cm}}\right)^{-1} \right. \\ \left. \times (1 - e\cos(\epsilon))^{-1}\right)^{8\beta/7}.\end{aligned} \tag{34}$$

With $a = 6 \times 10^{12}$ cm for the fiducial values, the maximal electron energy pre-factor (in Equation (33)) reaches 6.8×10^{12} eV in the periastron. If we instead use the equatorial result derived in Equation (27), the maximal energy would read

$$\begin{aligned}\gamma_{\rm max}^{(eq)} = 2.7 \times 10^6 \left(\frac{\zeta}{0.1}\right)^{1/2} \left(\frac{B}{10^{14}\ {\rm G}}\right)^{5/14} \\ \times \left(\frac{\dot{M}_{{\rm acc},eq}}{10^{16}\ {\rm g\ s^{-1}}}\right)^{-3/7} \left(\frac{R_{ns}}{10^6\ {\rm cm}}\right)^{15/14} \\ \times \left(\frac{M_{ns}}{1.4\, M_\odot}\right)^{-3/14}.\end{aligned} \tag{35}$$

The maximal energy in this case is on the order of 1.3×10^{12} eV for the fiducial values. Note that the higher the accretion rate (or the lower the magnetic field), the lower the maximal energy. Of course, the smaller the value of the efficiency, ζ, which could also change along the orbit, the smaller the maximal energy. To be explicit, for an assumed value of $\eta = 0.01$ (e.g., Khangulyan et al. 2008), the maximal energy is reduced to 411 GeV. The turbulent region of the propeller shock would not let electrons achieve TeV energies.

6. DISCUSSION

In the previous sections we have discussed the consequences of having a magnetar in the LS I $+61°303$ system (or at least a high B, long P pulsar that can burst in the way described). This possibility was based on the following:

1. On the observational evidence for one very short flare observed by the *Swift*. The only remaining counterpart candidate X-ray source within an improved 1σ uncertainty in position is LS I $+61°303$.
2. On the complete similarity of the previous event with all of the properties known for other magnetar flares.
3. On the fact that the longer flares observed by other satellites (and undoubtedly coming from LS I $+61°303$, having timescales of about 1 hr) are uncorrelated with harder X-ray emission, so discarding the shorter flare is a result of a strong spectral evolution of a typical non-magnetar burst (proven by an uncorrelated *Swift*/BAT or *RXTE*/HEXTE detection in any of the longer flares).

If we are to accept that a magnetar may be part of the LS I $+61°303$ system (which would be the first such discovery), we conclude from the analysis in the previous section that it would likely be subject to a flip-flop behavior. It would shift from behaving as a neutron star that is rotationally powered near the apastron to being a propeller near the periastron along each of the system's orbit.

Based on the preliminary analysis of the *Swift*/BAT burst reported in the Astronomer Telegrams (De Pasquale et al. 2008; Barthelmy et al. 2008; Dubus & Giebles 2008), earlier considerations of LS I $+61°303$ being formed by a magnetar have been made (Bednarek 2009; Dubus 2010). In them, the system has not been proposed to flip flop on any behavior, and the influence of the orbit was not considered. Dubus (2010) proposed that the system would always behave as a normal pulsar, mimicking in all respects the properties sustained by an interwind shock (e.g., as in Dubus 2006a). He also proposed that the short burst suggested a magnetic field strength of 10^{15} G, which we do not find justified. Instead, Bednarek (2009) proposed that the LS I $+61°303$ system is always a propeller, even in the apastron. We find that neither of these possibilities seems likely for typical magnetar parameters.

The idea of a flip-flop behavior for a neutron star in an eccentric orbit was considered earlier (see, e.g., Illarionov & Sunyaev 1975; Gnusareva & Lipunov 1985; Lipunov 1987; Lipunov et al. 1994; Campana et al. 1995), and a flip-flop behavior was even proposed for LS I $+61°303$ itself (Zamanov 1995; Zamanov et al. 2001). Although the idea was quickly abandoned in the literature, perhaps because of ms-pulsars, the system would indeed always be rotationally powered. In this work, we have rekindled some of these ideas but given them an extra edge. Prompted by the observational analysis, the LS I $+61°303$ pulsar has magnetar parameters and, thus, the flip-flop behavior is rather an expected outcome of the orbital evolution. But, perhaps the flip-flop behavior is in qualitative agreement with the remaining multi-wavelength phenomenology of the system.

6.1. A Flip-flopping Magnetar Model for LS I +61°303 in the Context of Multi-wavelength Observations

6.2. TeV Range

The TeV emission of the LS I +61°303 system has been discovered by MAGIC (Albert et al. 2006). A claim of periodic recurrence of the TeV emission was made thereafter, with the system showing regular outbursts at TeV energies in a broad range of phases around 0.65 (radio phases, such as in Gregory 2002, where the periastron is at phases 0.23–0.3, see, e.g., Casares et al. 2005; Grundstrom et al. 2007), with no significant signal elsewhere (Albert et al. 2009). The VERITAS array did independent observations and soon confirmed the MAGIC detection (Acciari et al. 2008, 2009). In addition, the MAGIC collaboration claimed a correlated X-ray/TeV emission at the position of the outburst (Anderhub et al. 2009) that would emphasize the common likely origin of the radiation in both bands. However, this was based on 60% coverage of only one orbit, and no one knew how general this result really was.

Neutron–star-based models presented to analyze the TeV emission from LS I +61°303 would produce a recursive orbital behavior, unless significant parameters (e.g., those defining the level of absorption) change in an orbit-to-orbit basis for reasons as yet unknown (see, e.g., Dubus 2006b, 2010; Sierpowska-Bartosik & Torres 2007, 2008, 2009; Bednarek 2009). The strong dependence on the system's geometry and the orbital position shown by the absorption and emission process (the pair production and anisotropic inverse Compton scattering) would produce an orbit-to-orbit–recurrent TeV burst. However, the peak of the TeV emission found by early measurements of MAGIC and VERITAS at radio phase 0.6–0.7 is not strictly near the superior conjunction of the orbit, which is where the conditions would be more favorable for gamma-ray production. Additional considerations were made to correct for this displacement in these models. Dubus et al. (2010) considered the influence of a relatively mild Doppler-boosted emission; assuming that there is an outflow velocity of 0.15–0.33 c, which is consistent with the expected flow speed at the pulsar wind termination shock. Sierpowska-Bartosik & Torres (2009) assumed that the light curve is generated by a variable power in the injection of relativistic particles.

Nevertheless, new observations by VERITAS (Acciari et al. 2010) discard the regularity of the TeV burst and the X-ray/TeV correlation. The observing seasons from 2008 to 2010 covered a total of eight orbits out of 27 available. The system was not detected in any of the orbits where it was earlier expected, near the apastron. Actually, in seven out of the eight orbits the system was not detected in any phase. As discussed by Acciari et al. (2010), arguing for shorter observation times cannot be accommodated. The imposed upper limit was less than 5% of the Crab Nebula flux, which is in the same energy range, in contrast to previous observations by both MAGIC and VERITAS that detected the source during these phases at 16% of the Crab Nebula flux. This implies that the system is in a low TeV state where the flux is at least a factor of three lower than the one detected in the 2006 observing season. Additionally, VERITAS reported that the system was significantly detected just once during observations taken in late 2010 at a phase much closer to the periastron passage.

In the scenario of this paper, the usual appearance of the TeV emission near the apastron would be explained under common lore: the interwind shock produced by the interaction of a rotationally powered pulsar and the stellar wind of the star accelerates particles, which in turn emit gamma rays. Instead, the common disappearance of the TeV emission in the periastron is accommodated by the fact that, on the one hand, the energy cutoff for the particle acceleration in the shock formed in the propeller regime is sub-TeV (and will be less for a larger accretion rate, a smaller magnetic field, and the expectedly smaller acceleration efficiency from the assumed fiducial values): and, on the other, the cross section for the pair production for any TeV particle is maximal. Typically, then, the system would appear and disappear where it has been observed along the 2006–2009 seasons.

Contrary to other models, the flip-flopping LS I +61°303 system could also provide a natural interpretation for the flux reduction or the total disappearance of the TeV radiation. If the mass-loss rate (and, thus, the accretion rate on to the neutron star) increases, the system quickly abandons its rotationally powered behavior, and, if it increases enough, it would not behave like that at any portion of the orbit. The interwind shock would not form and abundant TeV particles would not be produced. We note that even a small factor increase in the mass-loss rate at the apastron can cause the system to have a disrupted magnetosphere there (see Figure 9). (If the mass-loss rate of the equatorial outflow increases, its properties may change significantly, e.g., the truncation radius could be enlarged and even dominate at the apastron, which would also imply that significantly less TeV emission would be produced there.)

The orbit-to-orbit TeV changes can be understood in equal terms by directly linking them to the variations of the mass-loss rate in a highly variable behavior of Be stars. This has the obvious caveat of making a particular orbit's TeV light curve impossible to foresee, albeit that it links observations that are able to constrain the mass-loss rate with those at the highest energies, and it allows us to make a prediction about anti-correlation: the higher the mass-loss rate, the lower the TeV emission. If confirmed, these speculations about the detailed observations of this anti-correlation can impose constraints over the magnetar period.

6.3. The TeV Emission and Its Apparent Correlation with the Radio-obtained Super-orbital Phase

We now compare the year-long evolution of the system that was tracked in the radio and TeV energies, and we look at it from the perspective of the magnetar-composed LS I +61°303 model.

For the radio data we use the measurements compiled by Gregory (1999). Most of them are at a frequency of 8.3 GHz using the Green Bank Interferometer. The analysis of the radio emission led to the discovery of a super-orbital period at 1667 days (Gregory 2002). Figure 14 shows these data folded with the super-orbital period. We also show all the superimposed super-orbital phase ranges where there were TeV observations (either by MAGIC or by VERITAS) that covered the orbital phases where the LS I +61°303 system was initially detected near the apastron, i.e., at a broad radio phase around ∼0.65. All of the colored boxes in Figure 14 represent the TeV observations that covered the broadly defined apastron region of the LS I +61°303 orbit. Typically, several orbits are included in each of the colored boxes. In order to plot these TeV observations in Figure 14, the MJD of each observation time that covered the apastron region

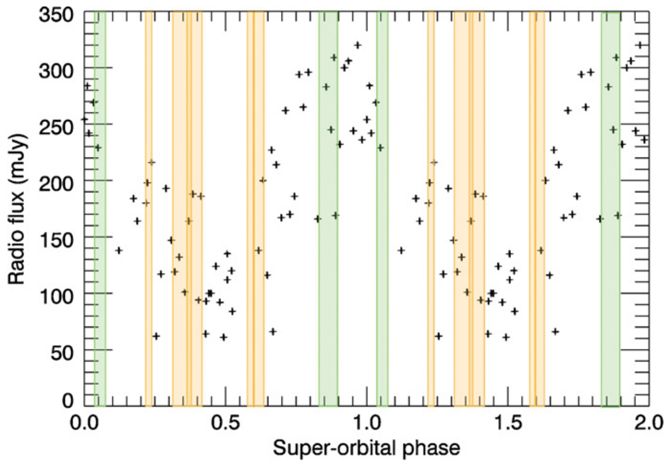

Figure 14. Radio data from LS I $+61°303$ compiled by Gregory (1999). Most of these are at a frequency of 8.3 GHz and folded with the super-orbital period of 1667 days. The colored boxes represent the MAGIC and VERITAS observation times that covered the broadly defined apastron region of the LS I $+61°303$ orbit. Light yellow boxes indicate periods in which the LS I $+61°303$ system was detected, and the light green boxes depict those in which it was not, implying at least a factor of three reduction in flux. Each of the boxes represents several orbits of LS I $+61°303$. Two super-orbital cycles are shown for clarity.

(A color version of this figure is available in the online journal.)

was obtained from all of the TeV reports on LS I $+61°303$ (Albert et al. 2006, 2009; Anderhub et al. 2009; Acciari et al. 2008, 2010) and converted into a super-orbital phase using the period of 1667 days. Although it is sparse, we note that the TeV coverage of the source goes from 2006 to 2010.

We see from Figure 14 that the system has appeared as a significant TeV source near the apastron only (light yellow boxes) at the super-orbital phases near the minimum of the radio flux. Instead, at the maximum of the radio flux, i.e., at the super-orbital phases near $\sim$0, the observations confirmed TeV upper limits only (green colored boxes). The latter situation corresponds to the recent disappearance of the source as reported by VERITAS, signifying an important flux reduction. Needless to say, the radio data and the TeV measurements are not contemporaneous, and we will speculate that the average properties of the super-orbital period that produced the radio long-term modulation have been maintained since 2002 until the present to extract conclusions. This may not necessarily be true (see, e.g., Trushkin & Nizhelskij 2010), although the drift in the maxima of the radio peak seems very small (on the order of three days) to affect the reasoning.

It is possible that Figure 14 represents a clue to the nature of the source. If we follow the interpretation by, e.g., Gregory et al. (1989), Zamanov et al. (1999), and Gregory (2002) and accept that the super-orbital radio flux modulation is the result of a cyclical variation in the mass-loss of the Be star (the synchrotron radio power emitted is directly proportional to the relativistic particle density that likely scales with the mass-loss rate), the disappearance of the flux reduction of the TeV radiation at the peak of the radio emission can be accommodated as follows: in the magnetar model for LS I $+61°303$, the increase in the mass-loss rate leads to an increase in the accretion rate onto the compact object, where the pressure makes the magnetic radius similar and eventually less than the light cylinder and disrupts the magnetosphere even at the apastron. If so, the system stops behaving as a normal pulsar, stops driving a wind, and stops forming an interwind shock. Instead, LS I $+61°303$ acts as a propeller. As a result, it is not expected to produce a significant number of multi-TeV particles, and, thus, the TeV radiation is suppressed. As in the periastron, the system was already behaving as a propeller, so there is no significant TeV in any part of the orbit.

We note that the results of Figure 14 are model independent because they are only based on observational results (when there was a detection near the apastron and when there was none) and on the times in which these observations were taken. They are, however, difficult to accommodate in other models of the source (which are also not able to explain the short burst). On the one hand, under the disk–jet coupling assumption (e.g., Falcke & Biermann 1995), the increase of the mass-loss rate would enhance the power in the jet in a microquasar scenario. Thus, in a microquasar model, when the mass-loss and accretion rates increase, there should be more TeV radiation, not less. On the other hand, estimations of the variations in the mass-loss rate from the Be star are given as the ratio between the maximal and minimal values obtained either from radio emission (a factor of four was determined by Gregory & Neish 2002) or from Hα measurements, which span from a factor of 5.6 (Gregory et al. 1989) to 1.5 (Zamanov et al. 1999); in any case, they span a factor of a few. In a normal pulsar wind, i.e., the stellar-wind scenario, when the pulsar is not a magnetar, an increase in the mass-loss rate by a factor of a few does not change the behavior of the source (which can be verified using, for instance, Equation (15)); the system would always have a non-disrupted magnetosphere. In the interwind shock scenario with a normal pulsar as part of the system, there is no apparent reason for the disappearance or the significant reduction of the TeV emission, or for the apparent correlation of this reduction with the maximum of the mass-loss rate when it increases by a factor of a few. Instead, in the case of a magnetar in LS I $+61°303$, fiducial values of the involved magnitudes put the neutron star in a position of the phase space in which small changes in the mass-loss rate can produce regime changes, thus accommodating Figure 14.

6.4. GeV Range

The GeV emission from LS I $+61°303$ has been detected using LAT on board *Fermi* (Abdo et al. 2009a) at the orbital periodicity. Given the data of the first eight months of the mission, only a single spectrum averaged along the orbit could be obtained. A power law with an exponential cutoff at a few GeV was found to the best fit. The folded *Fermi* light curve peaked at the periastron passage. The anti-correlation of the phase of the maximum between the TeV and GeV can be understood as a result of inverse Compton scattering and pair absorption. With 2.5 yrs of *Fermi*-LAT data, more details have been obtained (see, e.g., Hadasch 2011 for preliminary reports). The spectral characterization of LS I $+61°303$ now allows for a fit of a power law with an exponential cut-off spectrum along each of the analyzed portion of the system's orbit (which is typically cut in halves). However, the differences between these spectra are not large, and they are on the order of a 20% in flux and within errors in the determination of the cutoffs. The LAT now detects emission up to tens of GeV, where as the prior data sets only led to upper limits. Due to the contemporaneous measurements by VERITAS, commented above, we now know that there is no evidence that suggests that the process responsible for the detected *Fermi*-LAT emission continues beyond the GeV cutoff. One of the most interesting results of this further *Fermi*-LAT campaign is the detection of an overall flux increase around 2009 March on the order of 30%. This flux change was accompanied by a significant decrease in the GeV light curve modulation, which was flattened since then. This flux change approximately coincides with the period of the TeV flux reduction.

Within the magnetar-composed, flip-flopping model of LS I $+61^{\circ}303$, the usual behavior of GeV emission, which is being modulated along the orbit and anti-correlated with the TeV emission, finds its place as mentioned before. The increase in the GeV luminosity, much like the one found after 2009 March, can be understood because of the increase of the accretion rate, which would, in turn, increase the energy reservoir and a fraction ends up in the GeV domain. If this is the case, the magnetar in LS I $+61^{\circ}303$ would be behaving as a propeller along more portions of the orbit, and then would eventually act as a propeller along all of it. One would qualitatively expect that the GeV emission would no longer be significantly modulated. Since it is the same process that generates the radiation all along the orbit (there is no more interwind shock), the GeV-modulated fraction would diminish and flatten, and the TeV emission would be simultaneously reduced.

6.5. X-Ray Range

Zhang et al. (2010), Torres et al. (2010), and Li et al. (2011) present what we know of the X-ray behavior of the source via long-term, year-long monitoring using the *INTEGRAL* and *RXTE* satellites. The latter is the richest data set, and it has been discussed and enlarged through the addition of several more orbits in Section 1. Flares in the ks timescale have been detected for a long time by different experiments (see references in the quoted papers) and they can be accommodated as local processes, e.g., through clumpiness in the stellar wind. Their interpretation would likely not be affected within the magnetar-composed LS I $+61^{\circ}303$ model. An outcome of the *RXTE* campaign is the discovery of the variability in the orbital profiles of the X-ray emission. A light-curve profile variability is seen from orbit to orbit through multi-year timescales, with the phase of the profile maximum also changing. Such a high degree of variability can certainly be more easily accommodated with a magnetar hosted by LS I $+61^{\circ}303$ than in other models. In the former, we have different processes at different places that contribute to the X-ray emission, already in an orbit-to-orbit basis. Which process dominates, and the phases at which they start to become dominant, can be altered by the random (in orbital timescales) and cyclical (in super-orbital timescales) variations of the accretion rate. The possible appearance of the super-orbital variability in X-rays and the accumulation of such data remain a matter of study.

6.6. Radio Range

The existence of periodic ($\sim$26.5 days) non-thermal radio outbursts has allowed us to determine a strong modulation in the amplitude occurring on a timescale of $\sim$4 yrs, which has been commented on above (see, e.g., Gregory 2002, and references therein). Cyclic variability in the Be star envelope has been proposed as a possible origin of the long-term modulation. This has been emphasized by an apparent correlation of the super-orbitally varying radio flux within the Hα line parameters; the latter also presents a super-orbital modulation within the same period, albeit that it is shifted in phase by about 400 days (e.g., Zamanov & Martí 2000). In terms of the flip-flopping magnetar model for LS I $+61^{\circ}303$, the outburst onset could represent the time of the transition of the neutron star from a propeller to normal pulsar behavior (see, e.g., Zamanov 1995). The discussion in Zamanov & Martí (2000) put the general features of this model into context with radio observations (note that the super-orbital period has been corrected from 1584 to 1667 days since that paper was published, and the analysis should be changed accordingly).

The Very Long Baseline Array (VLBA) imaging obtained by Dhawan et al. (2006) over a full orbit of LS I $+61^{\circ}303$ has shown that the radio emission comes from angular scales smaller than about 7 micro-arcsec (which is the projected size of 14 AU at an assumed distance of 2 kpc). This radio emission appeared cometary-like, and it was interpreted to be pointing away from the high-mass star and, thus, the "smoking gun" of a pulsar wind. These results were found to be consistent with observations by the MAGIC collaboration, simultaneously using the Multi-Element Radio Linked Interferometer Network in the UK, the European Very Long Baseline Interferometry Network, and VLBA in the USA (Albert et al. 2008). The comparison between the Dhawan et al. (2006) and Albert et al. (2008) images at the same orbital phase (but obtained 10 orbital cycles apart) shows a high degree of similarity on both its morphology and flux, which suggests a certain stability of the physical processes involved in the radio emission. The tail is not always seemingly pointing in the *right* direction, as pointed out, for instance, by Romero et al. (2007) or Zdziarski et al. (2010), who noted that a high spin-down power pulsar would generate a wind that should overcome the stellar wind power and generate a flat interwind shock or even wrap it around the Be star, not the pulsar. Morphology-wise, the flip-flopping model may alleviate this problem, since even for a high $\dot{E}$ pulsar, there is no pulsar wind when a propeller is running and the high-energy emission is not coming from the interwind shock. The analysis of the conical shape of the radio emission would not apply. The MHD simulations of accretion onto a magnetized neutron star in the propeller regime have been recently presented by Romanova et al. (2003) and Toropin et al. (2006). Their simulations showed that the accreting matter is expelled from the equatorial region of the magnetosphere moving away from the star in a supersonic, disk-shaped outflow. Whether this outflow may be related to the radio morphology is still an open question.

6.7. Absence of Pulsations at All Frequencies

Finally, we remark that it is natural to expect a failure in detecting pulsations from a magnetar-composed LS I $+61^{\circ}303$ system. Radio pulsations are not common in magnetars. A few examples of radio-pulsed emission were detected mostly in connection with the outbursts of a few transient objects (Camilo et al. 2006, 2007; Levin et al. 2010), but this is far from being a common or stable property of these highly magnetized neutron stars.

On the other hand, the apastron would be the only region of the orbit when, for values of accretion rate so permitting, the pulsar in LS I $+61^{\circ}303$ would have an unscathed magnetosphere. However, the stellar winds might have prevented radio pulsations from being detected because of the strong free–free absorption all over the orbit and/or the large and highly variable dispersion measure induced by the wind. This would be very similar to the case of PSR B1259−63, which, at an inter-stellar distance that has almost the same dimension of the major axis of the orbit of LS I $+61^{\circ}303$ (given the larger 3.4 yr orbit of that system), also does not show radio pulsations at the periastron. In X-rays the upper limits derived by Rea et al. (2010) using the *Chandra* observations at phases close to the apastron mimic the situation of PSR B1259−63 (see the discussion in Rea et al.

2011), where again no pulsation is found. Furthermore, X-ray pulsations from magnetars can have pulsed fractions as low as 4% (e.g., Mereghetti 2007), well below the $\sim$10% upper limit derived by Rea et al. (2010). The absence of X-ray pulsations can also be understood in terms of having an X-ray emission that may be dominated by the shock rather than being due to the emission from the pulsar magnetosphere. In the periastron, and, generally speaking, in all phases where matter enters the light cylinder, the magnetosphere is disrupted and the pulsating-radio emission is halted. X-ray pulsating emission, on the other hand, is also halted in this case because the accreting matter does not reach the surface of the neutron star.

7. PREDICTIONS AND OUTLOOK

We can summarize a few testable predictions that are inherent to the scenario we have presented. Some of them are precise, and some represent trends on which further study may shed light on the validity of the assumptions made.

1. If one can track the mass-loss rate evolution of the companion star in LS I $+61^{\circ}303$, the TeV emission will be anticorrelated with it. This would be valid at all timescales, e.g., both in an orbit-to-orbit basis and in longer super-orbital timescales.
2. If we assume the persistence in the time of the super-orbital radio modulation, and if the cyclical increase of the mass-loss rate of the Be star already produces a flip-flopping LS I $+61^{\circ}303$ system (as suggested by Figure 14), it would be natural to expect low TeV fluxes near the apastron for super-orbital phases of $\sim 1 \pm 0.2$.
3. Under the assumption of the maintenance of the cyclical behavior of the accretion rate as inferred by the (somewhat old) radio data, we predict that the system should already be visible by the TeV instruments. It has been in the high state since approximately 2010 May–June, which is when the system attained a super-orbital phase of 0.2 (there is no coverage of the apastron orbital phases at this epoch reported in Acciari et al. 2010), and it will disappear or the TeV emission will be severely lowered again at a super-orbital phase of $\sim$0.7–0.8 around 2012 October.
4. If there is ever a giant flare observed from the magnetar hosted in LS I $+61^{\circ}303$, it will allow the detection of a magnetar-like pulsating tail, which will give us a better idea for the rotational period of the neutron star.
5. When the TeV emission is back to normal (appearing near the apastron), it would be natural to expect that the GeV to TeV connection would be different from that in the periastron (this could not be tested yet since the TeV emission was reduced only eight months after the *Fermi* launch and an orbital-separated spectrum could not be derived with such a data set). In the apastron, the TeV-emitting electrons are present, which may lead to the appearance of a second component above 10 GeV in the *Fermi* data. This should be less visible in the periastron, where the maximal energy of the electrons is cut at lower energies by the losses of the synchrotron.
6. When the TeV emission is significantly reduced or it completely disappears along the orbit, including near the apastron, it would be natural to expect that the radio morphology should change because there is no pulsar wind in place; instead, the propeller is what drives it.

We emphasize that a real description of these processes is far from the simplistic approach presented in this paper. The transitions between the regimes are in fact not modeled, they will likely depend on how matter is accreted and on whether a temporary accretion disk is formed, as well as on many other details. These will probably only be resolved through numerical simulations. Rather, this paper should be taken as an exploratory work for the plausibility of the idea when confronted with the rich phenomenology of the system. Under these caveats, we have found that the flip-flop magnetar LS I $+61^{\circ}303$ model not only seems to be suggested by a close look at the short burst observed by *Swift*/BAT and, in general, at the X-ray variability, but the model also appears to qualitatively agree with all of the other multi-frequency observations of the system and may explain the long-term behavior of the TeV variability. This qualitative ability of the model to accommodate a wide variety of constraints, even where others seem to fail, encourages further study, and studies of accretion onto strongly magnetized systems may prove to be very useful.

We acknowledge support from grants AYA2009-07391 and SGR2009-811, as well as the Formosa Program TW2010005. N.R. is supported by a Ramon y Cajal Fellowship. P.E. acknowledges financial support from the Autonomous Region of Sardinia through a research grant under the program PO Sardegna FSE 2007–2013, L.R. 7/2007. This work was also subsidized by the National Natural Science Foundation of China (NSFC) via NSFC-10325313, 10521001, 10733010, 11073021, and 10821061, the CAS Key Project KJCX2-YW-T03, and the 973 program 2009CB824800. Y.P.C. thanks the NSFC for support via NSFC-11103020 and 11133002. We thank W. Bednarek, R. Dubois, G. Dubus, C. Neish, and A. Okazaki for useful comments. We also acknowledge the use of the public *Swift* and *RXTE* data obtained from the High Energy Astrophysics Science Archive Research Center provided by the National Aeronautics and Space Administration's Goddard Space Flight Center.

REFERENCES

Abdo, A., Ackermann, M., Ajello, M., et al. 2009a, ApJ, 701, 123
Abdo, A., Ackermann, M., Ajello, M., et al. 2009b, ApJ, 706, L56
Abdo, A., Ackermann, M., Ajello, M., et al. 2011, ApJ, 736, L11
Acciari, V. A., Aliu, E., Arlen, T., et al. 2009, ApJ, 700, 1034
Acciari, V. A., Aliu, E., Arlen, T., et al. 2010, ApJ, 738, 3
Acciari, V. A., Beilicke, M., Blaylock, G., et al. 2008, ApJ, 679, 1427
Aharonian, F., Akhperjanian, A. G., Aye, K.-M., et al. 2005, A&A, 442, 1
Aharonian, F., Akhperjanian, A. G., Bazer-Bachi, A. R., et al. 2006, A&A, 460, 743
Aharonian, F., Akhperjanian, A. G., Bazer-Bachi, A. R., et al. 2007, A&A, 469, L1
Aharonian, F. A., Belyanin, A. A., Derishev, E. V., Kocharovsky, V. V., & Kocharovsky, V. V. 2002, Phys. Rev. D, 66, 023005
Albert, J., Aliu, E., Anderhub, H., et al. 2006, Science, 312, 1771
Albert, J., Aliu, E., Anderhub, H., et al. 2008, ApJ, 684, 1351
Albert, J., Aliu, E., Anderhub, H., et al. 2009, ApJ, 693, 303
Anderhub, H., Antonelli, L. A., Antoranz, P., et al. 2009, ApJ, 706, L27
Aptekar, R. L., Frederiks, D. D., Golenetskii, S. V., et al. 2001, ApJS, 137, 227
Aragona, C., McSwain, M. V., Grundstrom, E. D., et al. 2009, ApJ, 698, 514
Barthelmy, S. D., Baumgartner, W., Cummings, J., et al. 2008, GCN Circ., 8215, 1
Bednarek, W. 2009, MNRAS, 397, 1420
Bondi, H., & Hoyle, F. 1944, MNRAS, 104, 273
Bongiorno, S. D., Falcone, A. D., Stroh, M., et al. 2011, ApJ, 737, L11
Bosch-Ramon, V., & Khangulyan, D. 2009, Int. J. Mod. Phys. D, 18, 347
Bosch-Ramon, A., Paredes, J. M., Romero, G. E., & Ribó, M. 2006, A&A, 459, L25
Bozzo, E., Falanga, M., & Stella, L. 2008, ApJ, 683, 1031
Camilo, F., Ransom, S. M., Halpern, J. P., et al. 2006, Nature, 442, 892
Camilo, F., Ransom, S. M., Halpern, J. P., & Reynolds, J. 2007, ApJ, 666, L93
Campana, S., Stella, L., Mereghetti, S., & Colpi, M. 1995, A&A, 297, 385

Casares, J., Ribas, I., Paredes, J. M., Martí, J., & Allende Prieto, C. 2005, MNRAS, 360, 1105
Castor, J. I., & Lamers, H. J. G. L. M. 1979, ApJ, 39, 481
Chernyakova, M., Neronov, A., Aharonian, F., Uchiyama, Y., & Takahashi, T. 2009, MNRAS, 397, 2123
Chernyakova, M., Neronov, A., Lutovinov, A., Rodriguez, J., & Johnston, S. 2006, MNRAS, 372, 1585
Corbet, R., Cheung, C. C., Kerr, M., et al. 2011, ATel, 3221
Davies, R. E., & Pringle, J. E. 1981, MNRAS, 196, 209
de Pasquale, M., Barthelmy, S. D., Baumgartner, W. H., et al. 2008, GCN Circ., 8209, 1
Dhawan, V., Mioduszewski, A., & Rupen, M. 2006, in Proc. VI Microquasar Workshop: Microquasars and Beyond, ed. T. Belloni (Trieste: POS), 52.1
Dickey, & Lockman 1990, ARA&A, 28, 215
Dubus, G. 2006a, A&A, 456, 801
Dubus, G. 2006b, A&A, 456, 80
Dubus, G. 2010, in ASP Conf. Ser. 422, High Energy Phenomena in Massive Stars, ed. M. Josep, L. L.-E. Pedro, & A. C. Jorge (San Francisco, CA: ASP), 23
Dubus, G., Cerutti, B., & Henri, G. 2010, A&A, 516, A18
Dubus, G., & Giebles, B. 2008, ATel, 1715
Duncan, R. C., & Thompson, C. 1992, ApJ, 392, L9
Esposito, P., Caraveo, P. A., Pellizzoni, A., et al. 2007, A&A, 474, 575
Evans, P. A., Osborne, J. P., Godet, O., et al. 2008, GCN Circ., 8211, 1
Falcke, H., & Biermann, P. L. 1995, A&A, 293, 665
Falcone, A. D., Grube, J., Hinton, J., et al. 2010, ApJ, 708, L52
Frail, D. A., & Hjellming, R. M. 1991, AJ, 101, 6
Gavriil, F. P., Gonzalez, M. E., Gotthelf, E. V., et al. 2008, Science, 319, 1802
Gavriil, F. P., Kaspi, V. M., & Woods, P. M. 2002, Nature, 419, 142
Gehrels, N., Chincarini, G., Giommi, P., et al. 2004, ApJ, 611, 1005
Gnusareva, V. S., & Lipunov, V. M. 1985, SvA, 29, 645
Gogus, E., Kouveliotou, C., Woods, P. M., et al. 2001, ApJ, 558, 228
Gogus, E., Woods, P. M., Kouveliotou, C., et al. 1999, ApJ, 526, L93
Gregory, P. C. 1999, ApJ, 520, 361
Gregory, P. C. 2002, ApJ, 575, 427
Gregory, P. C., & Neish, C. 2002, ApJ, 580, 1133
Gregory, P. C., Xu, H.-J., Bachhouse, C. J., & Reid, A. 1989, ApJ, 339, 1054
Grundstrom, E. D., Caballero-Nieves, S. M., Gies, D. R., et al. 2007, ApJ, 656, 437
Hadasch, D. (for the *Fermi*-LAT collaboration) 2011, presented at the 3rd Fermi Symposium, Rome, 2011, May 10-14 (http://fermi.gsfc.nasa.gov/science/symposium/2011/program/session11b/Hadasch_FermiSymp_r.pdf)
Hilditch, R. W. 2001, An Introduction to Close Binary Stars (Cambridge: Cambridge Univ. Press)
Hinton, J., Skilton, J. L., Funk, S., et al. 2009, ApJ, 690, L101
Illarionov, A. F., & Sunyaev, R. A. 1975, A&A, 39, 185
Israel, G. L., & Dall'Osso, S. 2011, in Astrophysics and Space Science Proceedings, High-Energy Emission from Pulsars and their Systems, ed. N. Rea & D. F. Torres (Berlin: Springer), 279
Israel, G. L., Romano, P., Mangano, V., et al. 2008, ApJ, 685, 1114
Johnston, S., Ball, L., Wang, N., & Manchester, R. N. 2005, MNRAS, 358, 1069
Johnston, S., Manchester, R. N., Lyne, A., et al. 1992, ApJ, 387, L37
Johnston, S., Manchester, R. N., McConnell, D., & Campbell-Wilson, D. 1999, MNRAS, 302, 277
Khangulyan, D., Aharonian, F. A., & Bosch-Ramon, V. 2008, MNRAS, 383, 467
Khangulyan, D., Hnatic, S., Aharonian, F. A., & Bogovalov, S. 2007, MNRAS, 380, 320
Kumar, H. S., Ibrahim, A. I., & Safi-Harb, S. 2010, ApJ, 716, 97
Kumar, H. S., & Safi-Harb, S. 2008, ApJ, 678, L43
Lamers, H. J. G. L. M., & Cassinelli, J. P. 1999, Introduction to Stellar Winds (Cambridge: Cambridge Univ. Press)
Levin, L., Bailes, M., Bates, S., et al. 2010, ApJ, 721, L33
Li, J., Torres, D. F., Zhang, S., et al. 2011, ApJ, 733, 89
Lipunov, V. M. 1987, Ap&SS, 132, 1
Lipunov, V. M., Nazin, S. N., Osminkin, E. Yu., & Prokhorov, M. E. 1994, A&A, 282, 61
Maraschi, L., & Treves, A. 1981, MNRAS, 194, 1
Marlborough, J. M., Zijlstra, J.-W., & Waters, L. B. F. M. 1997, A&A, 321, 867
Martí, J., & Paredes, J. M. 1995, A&A, 298, 151
Mennickent, R. E., Vogt, N., Barrera, L. H., Covarrubias, R., & Ramírez, A. 1994, A&AS, 106, 427
Mereghetti, S. 2007, Ap&SS, 308, 13
Mereghetti, S. 2008, A&AR, 15, 225
Mereghetti, S., Götz, D., Weidenspointner, G., et al. 2009, ApJ, 696, L74
Mirabel, I. F. 2006, Science, 312, 1759
Muñoz-Arjonilla, A. J., Mart, J., Combi, J. A., et al. 2009, A&A, 497, 457
Muñoz-Arjonilla, A. J., Zabalza, V., Martí, J., et al. 2008, ATel, 1740
Okazaki, A. T. 2010, Presented at the Workshop on Galactic Variable Sources, Heidelberg (http://www.mpi-hd.mpg.de/astrophysik/HEA/conferences/binary_heidelberg/pages/Talks/Okazaki_binary_workshop_2010.pdf)
Okazaki, A. T., Bate, M. R., Ogilvie, G. I., & Pringle, J. E. 2002, MNRAS, 337, 967
Okazaki, A. T., Nagataki, S., Naito, T., et al. 2011, PASJ, 63, 893
Okazaki, A. T., & Negueruela, I. 2001, A&A, 377, 161
Orellana, M., & Romero, G. E. 2007, Ap&SS, 309, 333
Orellana, M., Romero, G. E., Okazaki, A. T., & Owocki, S. P. 2007, in Proc., Boletín Asociación Argentina de Astronomía, ed. G. Dubner et al. (Córdoba, Argentina: AAA), 50
Paredes, J. M., Ribo, M., Bosch-Ramon, V., West, J. R., & Butt, Y. M. 2007, ApJ, 664, L39
Perna, R., & Pons, J. 2011, ApJ, 727, L51
Ray, P. S., Jacob, M. H., & Jacob, M. 2008, ATel, 1730
Rea, N., & Esposito, P. 2011, in Proc. First Session of the Sant Cugat Forum on Astrophysics, High-Energy Emission from Pulsars and their Systems, ed. N. Rea & D. F. Torres (Berlin: Springer), 247
Rea, N., Esposito, P., Turolla, R., et al. 2010, Science, 330, 944
Rea, N., Israel, G. L., Turolla, R., et al. 2009, MNRAS, 396, 2419
Rea, N., & Torres, D. F. 2008, ATel, 1731
Rea, N., & Torres, D. F. 2011, ApJ, 737, L12
Rea, N., Torres, D. F., Caliandro, A. G., et al. 2011, MNRAS, 416, 1514
Rea, N., Torres, D. F., van der Klis, M., et al. 2010, MNRAS, 405, 2206
Romanova, M. M., Toropina, O. D., Toropin, Yu. M., & Lovelace, R. V. E. 2003, ApJ, 588, 400
Romero, G. E., Okazaki, A. T., Orellana, M., & Owocki, S. P. 2007, A&A, 474, 15
Scargle, J. D. 1998, ApJ, 504, 405
Sidoli, L., Pellizzoni, A., Vercellone, S., et al. 2006, A&A, 459, 901
Sierpowska-Bartosik, A., & Torres, D. F. 2007, ApJ, 671, L145
Sierpowska-Bartosik, A., & Torres, D. F. 2008, Astropart. Phys., 30, 239
Sierpowska-Bartosik, A., & Torres, D. F. 2009, ApJ, 693, 1462
Skilton, J. L., Pandey-Pommier, M., Hinton, J. A., et al. 2009, MNRAS, 399, 317
Smith, A., Kaaret, P., Holder, J., et al. 2009, ApJ, 693, 1621
Tam, P. H., Huang, R. H. H., Takata, J., et al. 2011, ApJ, 736, L10
Thompson, C., & Duncan, R. C. 1993, ApJ, 408, 194
Thompson, C., Lyutikov, M., & Kulkarni, S. R. 2002, ApJ, 574, 332
Toropin, Yu. M., Toropina, O. D., & Lovelace, R. V. E. 2006, in Proc. YSC, Vol. 1, ed. A. Golovin & A. Simon (Kiev: Kyiv Univ. Press), 13
Torres, D. F. 2011, in Proc. First Session of the Sant Cugat Forum on Astrophysics, High-Energy Emission from Pulsars and their Systems, ed. N. Rea & D. F. Torres (Berlin: Springer), 531
Torres, D. F., Zhang, S., Li, J., et al. 2010, ApJ, 719, L104
Trushkin, S., & Nizhelskij, N. 2010, Poster at the 38th COSPAR Scientific Assembly 2010, Accretion on Compact Objects and Fast Phenomena in Multi-wavelength Era, E13-0075-10 (https://www.cospar-assembly.org/abstractcd/COSPAR-10/abstracts/data/pdf/abstracts/E13-0075-10.pdf)
Tueller, M., Baumgartner, W. H., Markwardt, C. B., et al. 2010, ApJS, 186, 378
Waters, L. B. F. M. 1986, A&A, 162, 121
Woods, P. M., Kaspi, V. M., Thompson, C., et al. 2004, ApJ, 605, 378
Woods, P. M., & Thompson, C. 2006, in Compact Stellar X-Ray Sources, ed. W. Lewin & M. van der Klis (Cambridge Astrophysics Series 39; Cambridge: Cambridge Univ. Press), 547
Zamanov, R. K. 1995, MNRAS, 272, 308
Zamanov, R. K., & Martí, J. 2000, Astron. Astrophys. Lett., 358, 55
Zamanov, R. K., Martí, J., Paredes, J. M., et al. 1999, A&A, 351, 543
Zamanov, R. K., Martí, J. M., & Marziani, P. 2001, arXiv:0110114
Zdziarski, A. A., Neronov, A., & Chernyakova, M. 2010, MNRAS, 403, 1873
Zhang, S., Torres, D. F., Li, J., et al. 2010, MNRAS, 408, 642